Ref. Ares(2024)3157284 - 30/04/2024

Project number: 101083899

Project Acronym: SHARP-sCO_2

D4.1 – Optimized design of the high temperature radial flow packed bed thermal energy storage

Date: 30.04.2024

Author: KTH

This project has received funding from the European Union's Horizon Europe research and innovation programme under grant agreement No 101083899. The content of publication is the sole responsibility of the author(s). The European Commission or its services cannot be held responsible for any use that may be made of the information it contains.

This project has received funding from the European Union's Horizon Europe research and innovation programme under grant agreement No 101083899.

Project contractual details

Project title	Solar Hybrid Air-sCO2 Power Plants
Project Acronym	SHARP-sCO2
Grant Agreement No.	101083899
Project start date	1-11-2022
Project end date	31-10-2025
Duration	36 months
Website	https://www.sharpsco2.eu/

Deliverable details

Number	4.1
Title	Preliminary Design of high temperature radial flow packed bed TES
Work Package	4
Dissemination level[1]	PU
Due date (M)	30-04-2024
Submission date (M)	30-04-2024
Deliverable responsible	KTH
Contributing author(s)	Konstantinos Apostolopoulos Kalkavouras (KTH), Silvia Trevisan (KTH), Andrea Lessio (RINA-C), Theodoros Lyras (CERTH)
Reviewer(s)	Silvia Trevisan (KTH)
Final review and quality approval	30-04-2024

DOCUMENT HISTORY

DATE	VERSION	NAME	CHANGES
14.04.2024	1.0	Konstantinos Apostolopoulos Kalkavouras	Initial Draft
26.04.2024	1.1	Andrea Lessio (RINA-C), Theodoros Lyras (CERTH)	Initial draft of RINA-C and CERTH contributions
30.04.2024	2.0	Silvia Trevisan	Revised draft and final version

[1] PU = Public
CO = Confidential, only for members of the consortium (including Commission Services)

EXECUTIVE SUMMARY

This deliverable reviews the state of the art of high temperature thermal energy storages and describes the current state of work on the preliminary design of the high temperature radial flow packed bed thermal energy storage as part of WP4. This includes a summary of the considered boundary conditions to fit the targeted performance of the storage prototype and up-scaled unit fully accounting for the cyber-physical lab integration and relative limitations and capabilities of the experimental facilities. Existing high temperature packed bed thermal energy storage design concepts are reviewed and the proposed innovative storage concept is introduced highlighting how it targets shortcomings and drawbacks of state of the art solutions. The methodology and modelling approach followed to preliminary evaluate, via 0-1D models, the thermo and hydrodynamic performance of the storage is described. The influence of the key design parameters such as the relative thickness of the introduced coaxial layers, different particle sizes, and aspect ratio (ratio between the storage height and diameter) have been investigated. Pressure drop, useful charge and discharge operation and thermocline thickness have been considered as the main performance indicators. The results show that following a multi-objective optimization approach and looking at the expected trade-off between thermal and pressure drop related indicators sets of optimally equivalent storage designs can be identified. The relative thickness of the layers has a major influence directly affecting both the pressure drop and the useful operation time.

Detailed CFD/FEM modelling methodologies and key outcomes are presented summarizing the main TES performance and the TES geometry optimization aimed at maximizing the flow uniformity and distribution whilst ensuring limited thermal deformations.

All the above led to the finalized TES prototype definition and specifications which are summarized in the report also including detailed drawings.

Additionally, preliminary lab integration layouts, prepared as a basis for the upcoming lab adaptation and experimental campaign in WP4 are described. The proposed lab rig layout also ensures a full agreement with the cyber-physical lab approach and transferability of the results based on comparable boundary and working conditions among the three involved laboratories.

Finally, preliminary storage upscaled solutions are described and have been considered during the initial phases of the project to ensure scalability of the lab prototype and relevance of the experimental campaign results toward large-scale units.

This work is a steppingstone toward prototyping and validation work which will be carried on in the next tasks of WP4.

ABBREVIATIONS

BV: Butterfly Valve

CFD: Computational Fluid Dynamic

CH: Charge

DISCH: Discharge

EH: Electric Heater

HTC: Heat Transfer Coefficient

HTF: Heat Transfer Fluid

LR: Layer Ratio

LV: Low Voltage

MV: medium Voltage

PCM: Phase Change Materials

PBTES: Packed Bed Thermal Energy Storage

TES: Thermal Energy Storage

TABLE OF CONTENTS

1. INTRODUCTION

The overall scope of the SHARP-sCO2 project is to develop and validate key enabling components (receiver, storage, heat exchanger, and electric heater), proving the effectiveness and techno-economic viability of air solar-driven/sCO2 CSP plants able to be efficiently hybridized with PV in order to maximise CSP flexibility, reduce CAPEX and LCOE, whilst reducing the environmental impact. Four prototypes, one per key component, are investigated in a cross-fertilizing lab campaign (up TRL5) based on a cyber-physical lab integration approach.

The SHARP-sCO2 CSP plant main schematic layout is shown in Figure 1. WP4 focuses on the thermal energy storage (TES) and electric heater (EH) development and validation. This report targets the specifics of the TES preliminary design.

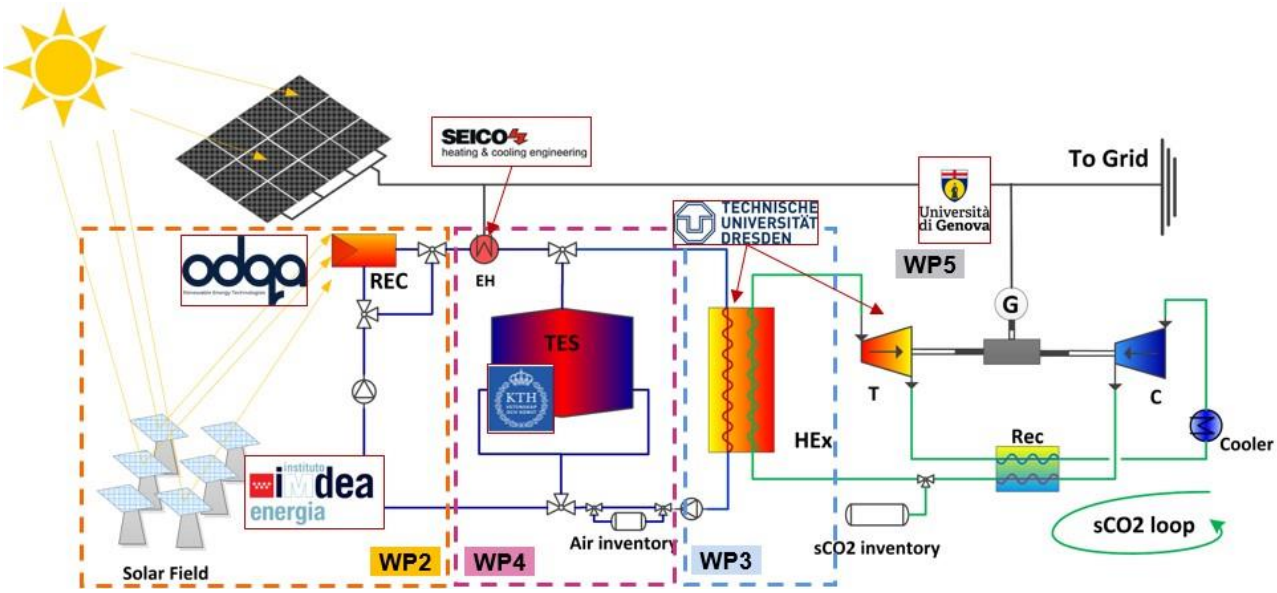

FIGURE 1: SHARP-SCO2 MAIN LAYOUT

1.1. CYBER-PHYSICAL LAB BOUNDARY CONDITIONS

To ensure replicability and transferability of the TES design and later experimental campaign, key boundary conditions to be considered have been defined in agreement with all relevant partners (Cyber-physical lab Committee). Further details are provided on D5.1, while table summarizes the boundary conditions relevant to the TES preliminary design.

TABLE 1: MAIN BOUNDARY CONDITIONS FOR TES PRELIMINARY DESIGN BASED ON SHARP-SCO2 CYBER-PHYSICAL LAB

Parameter	Value	Unit
TES energy capacity	50	kWh
TES power min/max (design)	0 – 50 (12)	kW
Air working temperature (min/max)	350 – 800	°C
Maximum air flow rate	0.12	kg/s
Air pressure	1+	bar

2. STATE OF THE ART HIGH TEMPERATURE PACKED BED THERMAL ENERGY STORAGE

Thermal energy storage (TES) will play a crucial role in the future energy sector. TES can provide high renewable penetration (such as in concentrating solar power (CSP) plant), ensuring dispatchable green power, as well as flexibility on the demand side with a smart management of the demand and enabling possibilities for waste heat recovery. Commercial large-scale TES units, developed for CSP applications, exploit solar salts and are limited to maximum temperatures lower than 580°C, due to thermal decomposition of the salt mixture. Solid based sensible TES can offer a technically viable and cost-effective alternative which could boost the exploitation of TES at higher temperatures, particularly when operated via a gaseous heat transfer fluid (HTF) [1]. Packed bed sensible TES (PBTES) systems store thermal energy by heating and cooling solid particles by means of a HTF that flows through the bed [2].

Several advantages of packed-bed TES concepts have been listed: cheap storing material; wide working temperature range; direct heat transfer between the HTF and the storing material; chemical stability with limited degradation and corrosion [2]. The main limitations of packed-bed TES have also been identified: pressure drop introduced by the filler material along the HTF flow; thermal losses to the surrounding environment; and thermal stratification degradation. Pressure losses are mostly affected by the size of the particle and the TES dimensions [3]. Thermal losses become particularly important during hold periods and they can lead to a reduction of more than 20% of the TES exergy content even at working temperatures around 150°C [4]. Minimizing the thermocline thickness can maximize the energy capacity of the storage, as well as its thermal performance [5]. The thermocline degradation is the flattening of the temperature gradient within the storage unit [6]. This phenomenon is caused by poor convective heat transfer coefficient between the HTF and TES material; thermal conduction and radiation; vorticity and bypass flows [6].

In previous research, different high-temperature packed-bed TES concepts have been proposed, and the most promising designs are shown in Figure 2. The traditional cylindrical tank with axial HTF flow (Figure 2.a) has been deeply investigated. The main drawbacks of this design are the elevated pressure drops, the high sensitivity to thermal ratcheting, high thermomechanical load on the tank, and the elevated thermal losses. The performance of this packed bed TES unit has been widely studied considering different ceramic materials (Al_2O_3 [4,7], ZrO_2 [8]) and working temperatures (from 100°C up to 900°C [9]). Maximum TES charge efficiencies of about 80% have also been measured [4]. The addition of a phase latent (PCM) layer at the top of the TES has also been experimentally studied [10], confirming its potential in stabilizing the TES outlet temperature during discharge as well as reducing the material cost for a given outlet temperature drop and increasing the TES exergy efficiency [11]. Zanganeh et al. proposed a buried truncated conical TES with axial HTF flow (Figure 2.b) [2]. The truncated conical shape reduces the thermal ratcheting by guiding the particles upwards. However, the thermal losses from the top surface are increased, as well as the capital expenditure due to the additional excavation cost [2]. Gauche et al. introduced a self-insulated unconstrained packed-bed TES concept, consisting of an unconstrained pile of rock packed-beds that surrounded central located rigid pipes with porous heat exchange regions at the bottom (Figure 2.c) [12]. This configuration, while cheap and self-insulated, is likely to lead to undesirable and unpredictable performance due to thermocline instabilities [13], linked to the unpredictability of the flow passage through the bed [14]. A layered parallel packed-bed with horizontal flow concept has been developed by Enolcon (Figure 2.d) [15]. The modular design enables the utilization of different materials in each layer, but flow uneven distributions have been measured [16]. A radial-flow packed bed TES design (Figure 2.e) has been proposed and tested by Trevisan et al. [17], confirming limited pressure drops and thermal losses during dwell. However, the temperature degradation and thermocline spread has been identified as the key drawback of this TES configuration limiting its efficiency to about 70 % for long operation cycles, while efficiencies higher than 90% were obtained in a similar TES unit for short cycles [18]. In radial flow packed bed TES, due to a variable cross sectional area, the majority of the pressure drop occurs in the inner section; while, the thermocline degrades more rapidly in the outer section.

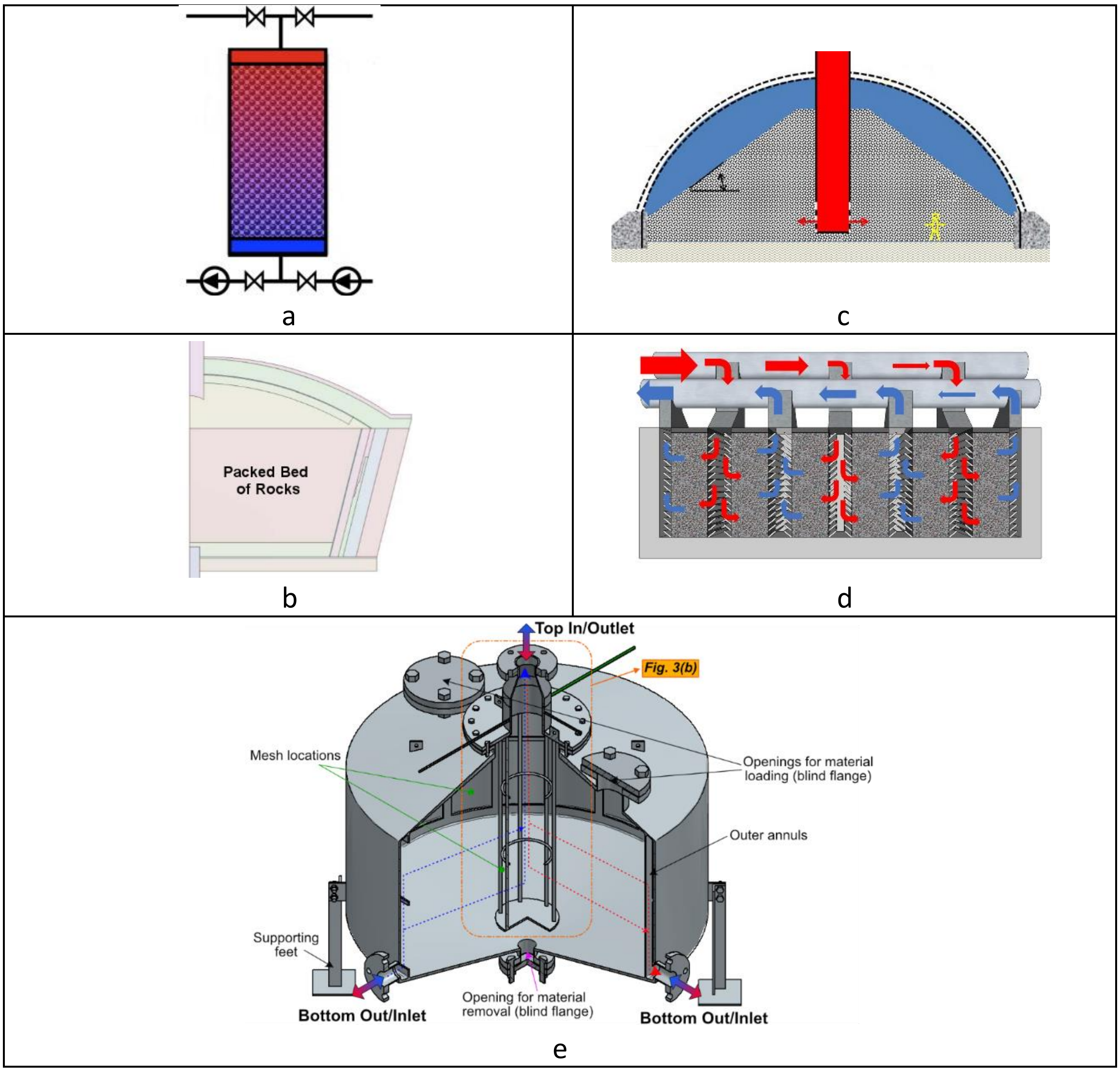

FIGURE 2. MAIN PACKED BED TES DESIGNS INVESTIGATED IN THE STATE OF THE ART OF THE TECHNOLOGY: (A) TRADITIONAL CYLINDRICAL PACKED BED TES WITH AXIAL HTF FLOW; (B) BURIED TRUNCATED CONICAL PACKED BED TES WITH AXIAL HTF FLOW [2]; (C) SELF-INSULATED UNCONSTRAINED PACKED-BED TES [12]; (D) LAYERED PARALLEL PACKED-BED TES WITH HORIZONTAL FLOW [15]; (E) RADIAL- FLOW PACKED BED TES [17].

To limit the thermocline degradation researchers have been proposing both passive and active methods. Passive methods affect the TES design and include increasing the TES aspect ratio (height to diameter ratio in traditional cylindrical packed beds) and the HTF to filler material heat transfer area by reducing the particle size [3]. Both methods, though enabling reductions of the thermocline degradation, increase the TES pressure drops. Active methods require to modify the operation of the TES, and includes strategies as flushing [19], siphoning [20], sliding ports [21], extracting/upgrading/returning [22]. These approaches have been investigated for cylindrical axial-flow segmented packed bed TES design. Thus, solutions to limit the thermocline degradation with limited negative influence on the pressure drop and with limited changes on the TES operation are deemed.

3. INNOVATIVE SHARP-sCO2 TES DESIGN CONCEPT

The 2D axis-symmetric geometry of the proposed innovative radial-flow segmented packed bed TES is sketched in Figure 3. Innovatively, with respect to the design in Figure 2.e, the TES comprehends annular coaxial packed bed segment. The specific example in the figure includes three sections S1, S2, and S3; however a detailed modelling and preliminary optimization analysis will look into the benefits of two versus three layers solutions. It is foreseen that the laboratory prototype will include two annular layers, while up-scaled solutions will benefit from three layers. During charge, the HTF would enter from the inner central pipe, flow radially outwards, be collected in the outer annulus and exit from the lower outlet port. During discharge instead the HTF path would be reverted. At the top of each segment, dedicated filler material loading ports are installed to facilitate the loading of the TES filler material. Similar ports are present on the bottom to permits filler removal. In homogeneous single material radial flow packed bed TES, the HTF speed is higher in the inner region of the TES due to smaller cross-sectional area. Different HTF flow speed along the radial direction leads to an uneven development of the pressure drops and thermocline. The majority of the pressure losses occurs in the inner section, where higher flow speed are registered. Contrarily, the thermocline is affected by the effectiveness of the heat transfer between HTF and solids. Thus, the thermocline degrades more rapidly in the outer section of the TES. From a TES design perspective, pressure drops and thermocline degradation limitations typically requires contrasting approaches leading to critical trade-offs. The proposed TES configuration could reduce the thermocline degradation enabling high thermal efficiency, utilization factors, and cost effective energy storage unit.

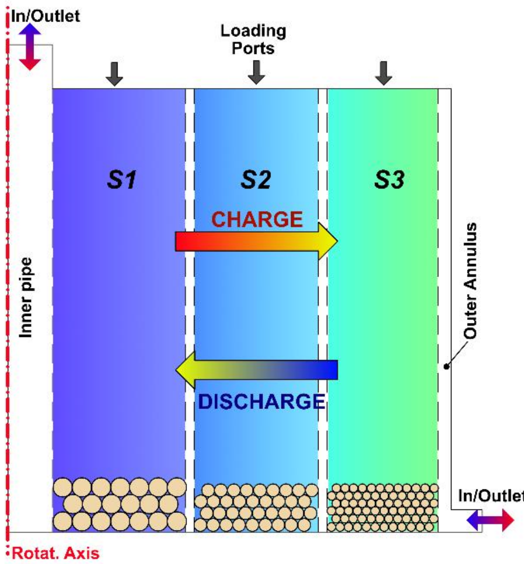

FIGURE 3. PROPOSED RADIAL-FLOW PACKED BED TES GEOMETRY SKETCH

In particular, the following aspects can be highlighted:

- The different segments can be filled by different materials, addressing specific performance requirements. In future, also the introduction of PCMs layers could be considered and enabled by the proposed TES geometry to further stabilize the HTF temperature.
- The inner segment (S1) can be filled with larger particles (diameter of about 10-12 mm). In this section, due to the lowest cross-sectional area the HTF velocity is high, ensuring good heat transfer with the filler. The heat transfer area can be reduced, by increasing the particle size, without compromising the effectiveness of the heat transfer but reducing the pressure drop.
- The outer segment (S3) can be filled with smaller particles (diameter of about 3-4 mm). In this section, due to the largest cross-sectional area the HTF velocity is low, guarantee low pressure drop, but causing wide thermocline spread. The small particle diameter can: increase the heat transfer

area between filler and HTF improving the convective heat transfer, hinder the effective thermal conductivity increase at high working temperature limiting thermal conduction.

- The thin annular air gaps would further hinder thermal conductivity between the different segment, reducing the thermocline degradation.
- The segmentation, and the different loading ports, would facilitate the filler material loading procedure, guaranteeing higher uniformity in the porosity distribution. This will limit by-pass flow issues highlighted in different packed bed TES units [6,17].
- The segmented TES design could innovatively permit to test the effectiveness of active thermocline control methods in radial-flow configurations.

4. TES THERMODYNAMIC PERFORMANCE INVESTIGATION

To identify a PBTES design to be prototyped the described TES and particularly its thermodynamic and thermomechanical behaviour have been modelled. The main modelling approach and its key outcomes are described in the sections below. The modelling approach covers both 1D two phases for multi-objective TES design optimization and detailed CFD/FEM for specific modelling of some key features of the unit.

4.1. MODELLING APPROACH

The thermodynamic behavior of the PBTES has been described by adapting the Schumann model [23] to the radial geometry. Specifically, the 1D two phases model can be summarized by Eqs. (1) and (2). Specifically, Eq (1) describes the fluid temperature, T_F, while Eq. (2) describe the solid temperature, T_S.

$$\frac{\partial T_F}{\partial t}+\frac{G}{\varepsilon\rho_F}\frac{\partial T_F}{\partial r}=\frac{k_{F,eff}}{\varepsilon\rho_F c_{p,F}}\left(\frac{1}{r}\frac{\partial}{\partial r}\left(r\frac{\partial T_F}{\partial r}\right)\right)+\frac{ha_s\left(T_S-T_F\right)}{\varepsilon\rho_F c_{p,F}}+\frac{U_w\left(T_\infty-T_F\right)}{H\varepsilon\rho_F c_{p,F}} \tag{1}$$

$$\frac{\partial T_S}{\partial t}=\frac{k_{S,eff}}{(1-\varepsilon)\rho_s c_{p,S}}\left(\frac{1}{r}\frac{\partial}{\partial r}\left(r\frac{\partial T_S}{\partial r}\right)\right)+\frac{ha_s}{(1-\varepsilon)\rho_s c_{p,S}}\left(T_F-T_S\right) \tag{2}$$

Key parameters are the heat transfer coefficient between the solid filler material and the fluid flow, h, and the effective thermal conductivities for the two phases, $k_{F,eff}$ and $k_{S,eff}$. The convective HTC between the HTF and the filler material governs the charge and discharge processes and the TES stratification. It has been evaluated, in its classical surface form [W/(m²·K)], by means of the correlation proposed by Coutier and Faber [24], Eq. (3). The shape factor, $a_s = A_s/V_b = 6(1-\varepsilon)/d_p$, enables to transpose h in the volumetric form. The Coutier and Faber's correlation was obtained via different experimental setups, and several minor phenomena are already considered in it, avoiding further modeling efforts. Various other correlations to evaluate the convective HTC have been suggested [25], providing comparable results.

$$h=\frac{700}{6(1-\varepsilon)}G^{0.76}d_p^{0.24} \tag{3}$$

The effective, temperature dependent, thermal conductivity of the packed bed, k_{eff}, has been calculated as from [26]. Various other correlations have been presented providing similar results [25]. The effective thermal conductivity has been divided between the two phases based on the methodology presented in [27].

The pressure drop has been calculated via the Ergun equation as in Eq. (4) [28].

$$\frac{\Delta p_{TES}}{(R_{out}-R_{in})}=1.75\left(\frac{1-\varepsilon}{\varepsilon^{3}}\right)\frac{G^{2}}{\rho_{F}d_{p}}+150\left(\frac{(1-\varepsilon)^{2}}{\varepsilon^{3}}\right)\frac{G\mu_{F}}{\rho_{F}d_{p}^{2}} \tag{4}$$

The main investigated PBTES consists of two and three radial layers (inner and outer) at both a small lab scale (50 kWh) and an industrial scale (10MWh). The 2D axisymmetric sketch of the studied TES geometries are shown in **Error! Reference source not found.**. Four main design variables have been considered: the layer r atio (defined as the ratio $(R^{*}-R_{in})/(R_{out}-R_{in})$, where R^{*}, R_{in} and R_{out} are the radius of the layers separation, inner radius and outer radius, respectively), the inner particle diameter, the outer particle diameter, and the aspect ratio, defined as $\alpha = (R_{out}-R_{in})/H$. The design variables are also included in Figure 4, Table 3 summarizes the specific ranges considered for these decision variables in the optimization. Eqs. (1) and (2) describing the temperature profiles have been applied to both inner and outer layer considering a continuity boundary condition (same fluid and solid temperature) between the two layers. Similarly, the Ergun equation has been applied to both layers and the total pressure drop has been calculated as the sum of the pressure drop imposed by the inner layer and the one imposed by the outer layer. Additional TES sizing parameters considered in the modelling are summarized in Table 2, these values have been considered as fixed, later more comprehensive optimization studies in WP5 will assess their influence and verify these preliminary assumptions.

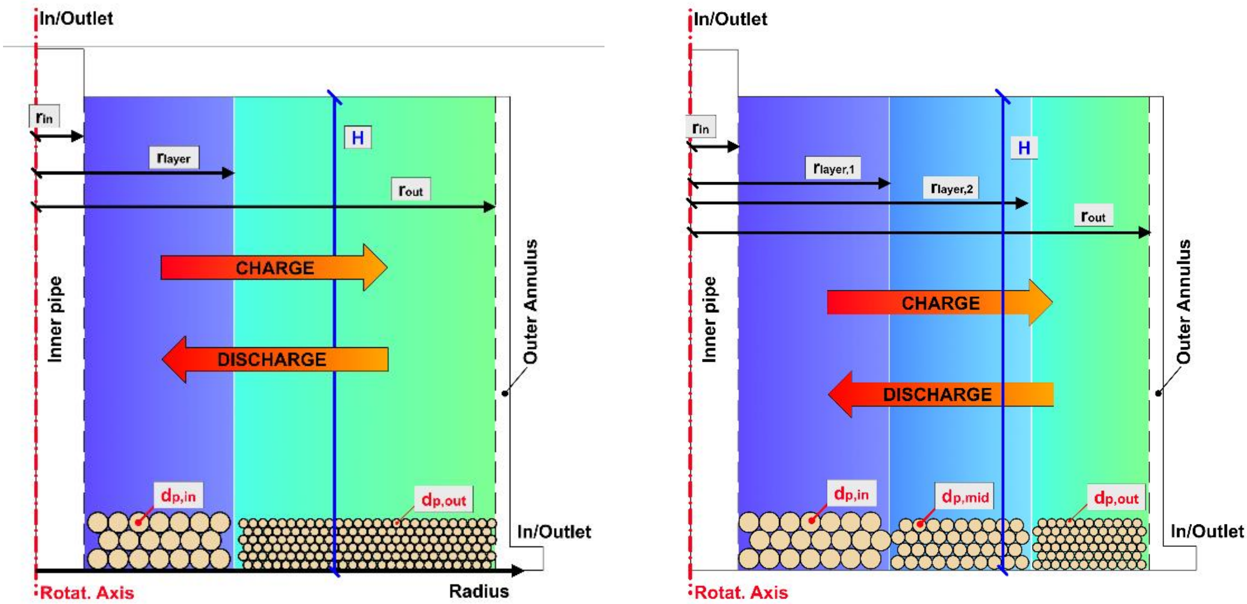

(a) (b)

FIGURE 4: 2D AXIS-SYMMETRIC REPRESENTATION OF THE CONSIDERED PBTES GEOMETRY AND MAIN DESIGN VARIABLES FOR A PBTES UNIT WITH 2 COAXIAL LAYERS (A) AND A PBTES UNIT WITH 3 COAXIAL LAYERS (B)

TABLE 2: ADDITIONAL SIZING PARAMETERS OF THE INVESTIGATED LAB SCALE PBTES

Parameter	Value (Ind.- Lab)	Unit
Energy capacity	10000 - 50	kWh
Temperature (min in discharge/max in charge)	200-800	°C
Power (charge/discharge)	4000 - 20	kW
Void fraction	0.38	-
Preliminary efficiency	0.85	-
TES volume	0.497	m^3

Four key performance indicators have been considered to describe and assess the TES thermodynamic performance:

- The pressure drop across the full packed bed TES
- The useful duration of charge and discharge, defined as the time at which the outlet fluid temperature reaches the cut-off value (T_{min}-100°C in charge or T_{max}-100°C in discharge),
- The maximum thermocline thickness.

Additionally, to evaluate the influence of each decision variable over the KPIs the different correlation coefficients, between each independent variable and the KPIs, have been calculated [29].

TABLE 3: VALUES AND CONSTRAINTS CONSIDERED FOR THE DESIGN DECISION VARIABLE IN THE TES DESIGN MOO. THE MAIN VALUES LISTED REFER TOT THE INDUSTRIAL SCALE TES UNIT (10MWH), WHILE THE VALUES REPORTED IN THE PARATHESIS REFER TO LABORATORY SCALE TES (50KWH).

Variable	Minimum	Maximum	Step	Unit
Inner particle diameter, $d_{p,in}$	60 (12)	100 (22)	10 (2)	mm
Mid particle diameter, $d_{p,mid}$	20 (4)	60 (10)	10 (2)	mm
Outer particle diameter $d_{p,out}$	5 (2)	20 (8)	5 (2)	mm
Layer ratio, LR	0.1	0.9	0.1	-
Layer ratio 1, LR_1	0.1	0.7	0.1	-
Layer ratio 2, LR_2	0.1	0.7	0.1	-
Aspect ratio, $\alpha = \Delta r / H$	0.5	2	0.5 (0.25)	-

4.2. THERMODYNAMIC TES PERFORMANCE

Initially the focus has been set on understanding the general thermodynamic performance of the TES unit and investigate the relevance of additional coaxial layers (two vs three). Figure 5 presents the HTF (solid lines) and solid (dashed lines) temperatures along the TES radial direction during charge (a) and discharge (b) at different time instants (after 10 minutes, 1 and 2 hours) for three different PBTES arrangements with two coaxial layers and LR equal to 0.1, 0.5 and 0.9. The presented results refer to a laboratory sized TES unit, and similar temperature profiles are attained by the upscaled industrial TES. The inner layer, filled with larger particles, is highlighted by the grey area in Figure 5. Similarly, Figure 6 presents the HTF (solid lines) and solid (dashed lines) temperature along the TES radial direction during charge (a) and discharge (b) at different time instants (after 10 minutes, 1 and 2 hours) for three different PBTES arrangements with three coaxial layers and different values of LR_1 and LR_2. The main sizing parameters of the TES units have been considered as for the base configuration listed in Table 2. The progressive flattening of the temperature curve during operation can be observed in all plots. The thermocline degradation is particularly relevant during discharge operation, during which flatter temperature curves can be observed leading to wider thermocline regions. The effect of particle size can be seen, for examples, by comparing the temperature behavior for a two coaxial layers PBTES configuration at LR = 0.1 and the one with LR = 0.9. Smaller particles grants larger heat transfer area between HTF and solid and higher heat transfer coefficients. This results in steeper temperature curves and thinner thermocline regions. This behavior can be observed also in the configuration with intermediate LR for which a change of the slope of the temperature curve in between two adjacent layers is visible. Additionally larger particle diameters also enlarge the temperature difference between the HTF and the solid due to a worsening of the heat transfer between HTF and solid. The introduction of a third additional coaxial layer, at least considering the specific particle sizes considered, does not affect largely the temperature profile with the PBTES units.

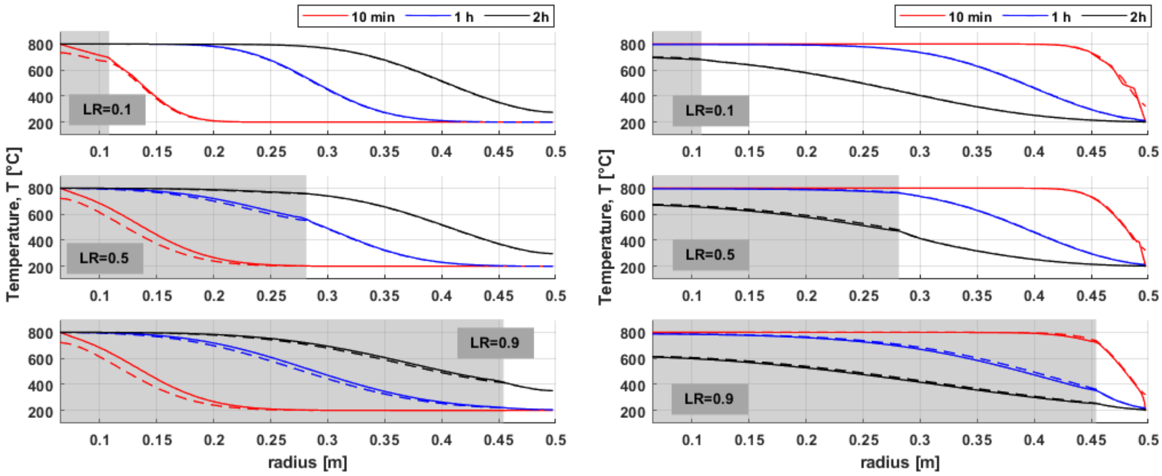

(a) (b)

FIGURE 5: (A) HTF (SOLID LINES) AND SOLID (DASHED LINES) TEMPERATURE PROFILE OVER THE 2 COAXIAL LAYERS PBTES RADIUS FOR DIFFERENT LR DURING CHARGE; (B) HTF (SOLID LINES) AND SOLID (DASHED LINES) TEMPERATURE PROFILE OVER THE PBTES RADIUS FOR DIFFERENT LR DURING DISCHARGE.

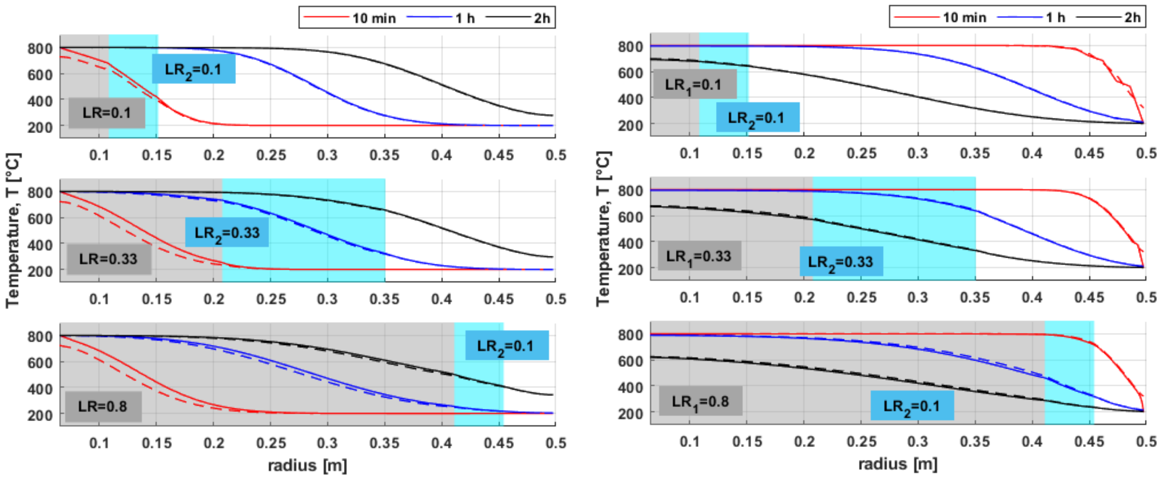

(a) (b)

FIGURE 6: (A) HTF (SOLID LINES) AND SOLID (DASHED LINES) TEMPERATURE PROFILE OVER THE 3 COAXIAL LAYERS PBTES RADIUS FOR DIFFERENT LR DURING CHARGE; (B) HTF (SOLID LINES) AND SOLID (DASHED LINES) TEMPERATURE PROFILE OVER THE PBTES RADIUS FOR DIFFERENT LR DURING DISCHARGE.

Figure 7 highlights the hydrodynamic behavior and pressure drop reduction potential attainable by the proposed PBTES design with two coaxial layers, for both the industrial 10 MWh TES unit (Figure 7(a)) and a 50 kWh prototype (Figure 7(b)). The total pressure drop and its share between the inner and outer layer is shown for three different PBTES arrangements with LR equal to 0.1, 0.5 and 0.9. Inner particle diameter ($d_{p,in}$) of 80 mm and outer particle diameter ($d_{p,out}$) of 20 mm have been considered for the 10 MWh TES, while $d_{p,in}$ equal to 20 mm and $d_{p,out}$ equal to 5 mm have been applied to the 50 kWh unit. Similarly, the total pressure drop of two radial flow PBTES with uniform particle diameter of 20 mm and 80 mm (or 5 mm and 20 mm in the downsized TES) is shown (to enable a better understanding of the pressure drop distribution along the radius for these two examples with uniform particle size distribution the share between inner and outer layer assumes a LR equal to 0.5). To provide a better overview, the total pressure drop of two similarly sized axial flow PBTES with unitary aspect ratio, defined as $\alpha_{AX} = H/D$, and uniform particle diameter of 20 mm and 5 mm is also presented. Figure 7 shows also the useful duration of charge and discharge operation for the different radial flow PBTES units considered. Firstly, it can be noted that the radial flow PBTES design ensures a pressure drop reduction of about 50% with respect to similar axial flow PBTES units, both in the industrial and downsized unit. The radial TES led to limited useful operation time reductions, generally below 6% in lab scale units, and below 1% for thermally effective large scale TES with small particles (i.e. AX 20 mm and RAD 20 mm). For larger particle size (i.e. RAD 80 mm) useful operation time reduction of about 15 % is recorded with respect to comparable axial flow PBTES. The layered design can attain further pressure drop reductions at the expense of limited operation time reductions. In radial flow PBTES with uniform particle size more than 75 % of the total pressure drop occur in the innermost 50 % of the TES radius, as showed by the bars RAD 20mm and RAD 80mm (or RAD 5 mm and RAD 20 mm for the prototype unit). This highlights the need to act on the inner section of the TES unit to limit the parasitic losses. As an example, introducing larger particles (80 mm diameter against the original 20 mm) in the inner 50 % of the TES (LR = 0.5) leads to a total pressure drop reduction of about 68 % with respect to the homogenous 20 mm particle radial flow PBTES, and about 83 % with respect to the homogenous 20 mm particle axial flow PBTES. When looking at the influence of the LR a parabolic trend can be noted, with larger relative Δp_{TES} reductions attainable at small LR. A plateau can be reached for high LR, meaning that when most of the PBTES is already filled with large particles a further increment of LR does not produce a relevant hydrodynamic performance enhancement. The trade-off between thermal and hydrodynamic performance is evident when looking also at the useful duration of charge and discharge. PBTES units with reduced Δp_{TES} have lower $t^*_{ch/disch}$. However, introducing larger particles in the inner 50 % of the TES would cause a reduction of the useful operation time of only 8 % for large TES units and 5 % for prototype TES, whilst providing a pressure drop reduction of about 70 % with respect to a radial flow PBTES with uniform small particle diameter. This example highlights that beneficial results could be attained by the proposed TES unit largely reducing pressure drop at the expense of limited reductions of the useful operational time. The reported useful operation time also shows that the downscale TES units is more largely affected by inefficiencies and thermal losses. The $t^*_{ch/disch}$ for a 50 kWh TES unit is in average about 9 % lower than the one for a 10 MWh PBTES. Figure 7 also indicates that for upscaled TES units the useful duration attained in charge and discharge are similar (with an average difference of 1.8 min), while an average difference of 7.4 min (equivalent to about 6% of the average useful duration) is reported for a 50 kWh PBTES. This shows that the inefficiencies during the TES operation affect more relevantly the discharge phase and this is more visible in laboratory scaled TES units.

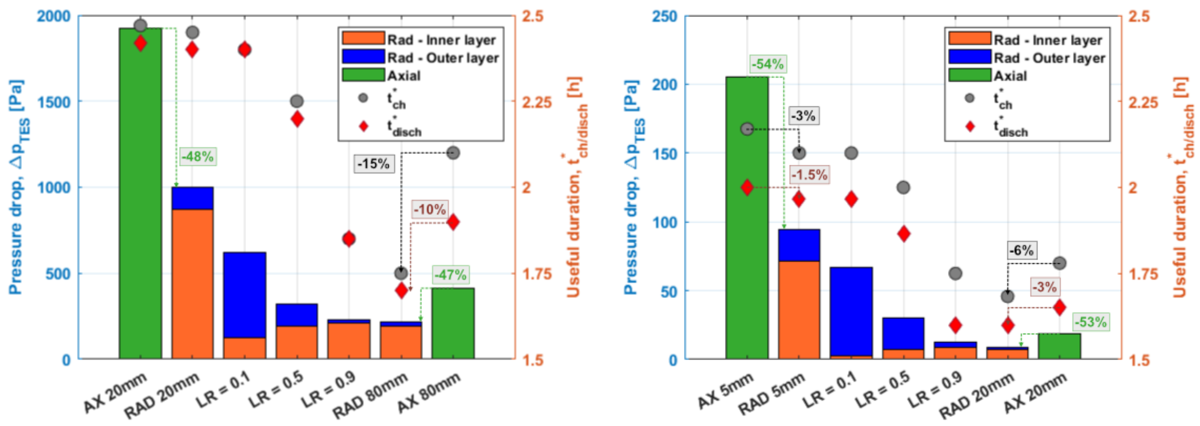

(a) (b)

FIGURE 7: PRESSURE DROP ACROSS THE PBTES FOR THE PROPOSED DESIGN WITH 2 COAXIAL LAYER, CONSIDERING DIFFERENT LR, AND A SIMILAR REFERENCE PBTES WITH AXIAL FLOW FOR A 10 MWH INDUSTRIAL UNIT (A) AND A 50 KWH LABORATORY SCALE UNIT (B).

Similarly, Figure 8 shows the pressure drop recorded for the proposed PBTES design with three coaxial layers, for a 10 MWh and a 50 kWh unit and considering a set of representative LR_1 and LR_2. The share of pressure drop in the different layers is also indicated together with the useful duration time both during charge and discharge. The wider the inner and intermediate layer the lower the total pressure drop. As visible also in Figure 7, for larger TES units, the inner layers are responsible for a larger share of the total pressure drop. By comparing the PBTES with two or three coaxial layers, it can be observed that the differences of both total pressure drop and useful durations are limited. Thus, a PBTES with two coaxial layers could represent a better alternative thanks to its simpler construction and it will be considered for the later stages of the TES unit design (both at upscaled and lab scale).

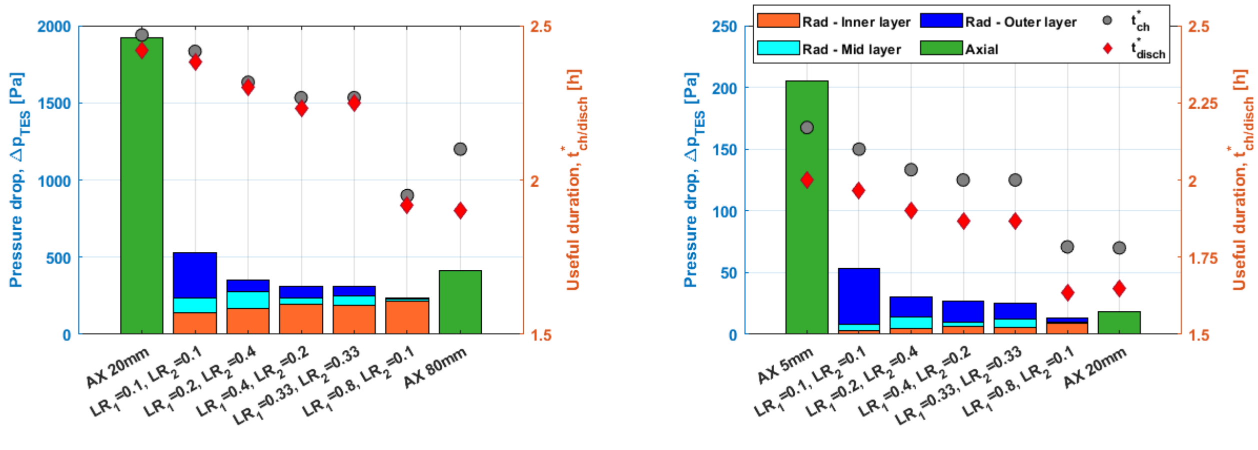

FIGURE 8: PRESSURE DROP ACROSS THE PBTES FOR THE PROPOSED DESIGN WITH 3 COAXIAL LAYERS FOR A 10 MWH INDUSTRIAL UNIT (A) AND A 50 KWH LABORATORY SCALE UNIT (B) CONSIDERING DIFFERENT REPRESENTATIVE LR1 AND LR2

In PBTES with uniformly distributed particle size most of the pressure drop occurs in the inner region due to higher flow speed caused by the smaller cross sectional area. In both TES configuration wit uniform particle size about 80% of the pressure drop is in the inner half while about 20% is localized in the outer half. Including larger particles in the inner layer shifts the drop contribution toward the outer layer and largely contributes to an overall pressure drop reduction. Even with only 25% of the radius filled with larger particles contributes to more than 50% pressure drop reduction. Based on the preliminary sizing a maximum useful duration (at 100% efficiency) of 4 hours could be expected. The layering and larger particle sizes worsen the thermal performance leading to shorter operations, particularly in discharge mode. However, it can be noted that for a TES configuration ensuring 50% pressure drop reduction the useful operation is shortened only by less than 1%. This highlights the potential of the proposed TES configuration.

4.2.1. TES Thermodynamic performance optimization

Figure 9 and Figure 10 show the Pareto fronts obtained from the PBTES design MOO for a 10 MWh and a 50 kWh unit, respectively. The configurations with two coaxial layers are shown in Figure 9(a) and Figure 10(a) while the units with three coaxial layers are shown in Figure 9(b) and Figure 10(b). The curves directly summarize the trade-off between pressure drop and useful duration of operation, during both charge and discharge. The color of the dots shows the maximum thermocline thickness measured during both operations. By comparing the plots, it can be observed that, as highlighted before, the addition of a third layer has a limited influence over the identified Pareto fronts and similar trends occur. This further confirms that layered PBTES with only two coaxial layers could serve the purposes whilst limiting construction challenges. In both TES sizes considered, the discharge phase suffers from wider thermocline spreads, due to the previously highlighted flatter temperature profiles in discharge operation. From Figure 9, it can be observed that for an industrial sized PBTES an increase in the useful duration $t^*_{ch/disch}$ corresponds to thinner thermocline thicknesses ΔTC and charge and discharge operation phases are characterized by similar useful durations. The target useful duration of 2.5 hours can be attained at a pressure drop lower than 500 Pa and at maximum thermocline thicknesses of about 0.3 during charge and 0.55 during discharge. The long attained useful operation translates in a maximum thermal efficiency of the TES unit of about 88%.

The laboratory scale PBTES unit is instead characterized by shorter useful operations, with a particular reduction for the discharge phase. This reduction translates also in a reduction of the TES thermal efficiency down to maximum values of about 76 % and 72% in charge and discharge, respectively. In charge operation useful duration longer than 2 hours are attained with thermocline thicknesses of about than 50%. Contrarily, in discharge operation the ΔTC measured along the Pareto front is always higher than 70%. PBTES configurations that cause high maximum thermocline spreads during discharge still ensure relatively high t^*_{disch} because in these units the thermocline spreads internally reaching the outlet at a late time. Thanks to this internal spread of the thermocline the outlet HTF temperature raises less rapidly ensuring sufficient t^*_{disch}. However, due to the poorer thermal performance achieved in discharge operation, in order to attain a useful duration of 2 hours a PBTES units causing higher pressure drops, about twice the values measured during charge, is required.

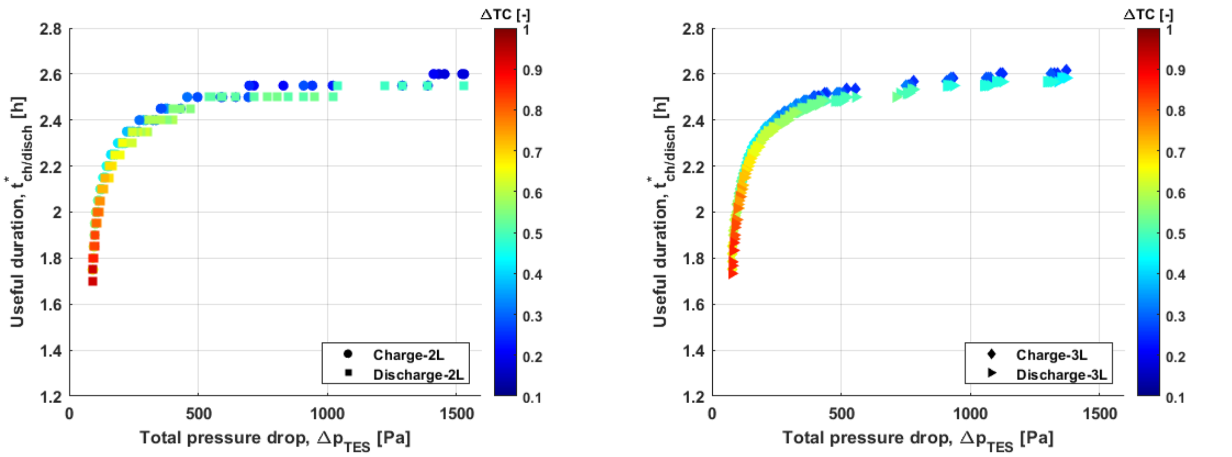

(a) (b)

FIGURE 9: PARETO FRONTS FROM THE MULTI-OBJECTIVE OPTIMIZATION OF THE KPIS (PRESSURE DROP AND USEFUL TIME OF CHARGE AND DISCHARGE) OF THE PROPOSED PBTES DESIGN WITH 2 COAXIAL LAYERS (A) AND WITH 3 COAXIAL LAYERS (B) (FOR AN INDUSTRIAL 10 MWH PBTES UNIT), ALSO SHOWING THE MAXIMUM THERMOCLINE THICKNESS.

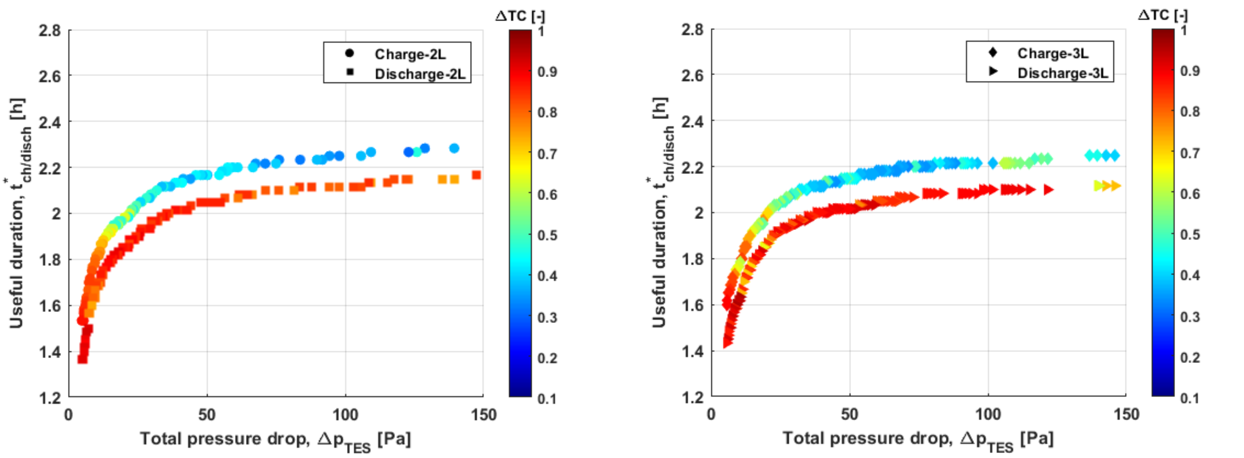

(a) (b)

FIGURE 10: PARETO FRONTS FROM THE MULTI-OBJECTIVE OPTIMIZATION OF THE KPIS (PRESSURE DROP AND USEFUL TIME OF CHARGE AND DISCHARGE) OF THE PROPOSED PBTES DESIGN WITH 2 COAXIAL LAYERS (A) AND WITH 3 COAXIAL LAYERS (B) (FOR A 50 KWH PBTES UNIT), ALSO SHOWING THE MAXIMUM THERMOCLINE THICKNESS.

The layer ratio LR and the aspect ratio α are the two most relevant design variables on the PBTES performance. Increasing the LR, meaning that larger sections of the PBTES are filled with bigger particles, causes reduced pressure drops but worse thermal performance. Lower pressure drops are ensured thanks to the lower HTF flow blockage effect of wider particles. Worse thermal performance is due to lower effective heat transfer areas and convective heat transfer coefficients in the regions with larger particles. For laboratory scaled units a large set of the Pareto front is characterized by LR higher than 0.5. In large scale applications, the pressure drop becomes more relevant; thus, TES configuration with low α and Δp_{TES} are preferred. To achieve such pressure drop reduction, the most relevant design parameter to act upon in industrial scale units is the aspect ratio, as testified also by a $r_{\alpha,\Delta p_{TES}}$ of 0.7 (against a $r_{LR,\Delta p_{TES}}$ of -0.24). Contrarily, in laboratory scaled units the LR has the largest influence with a $r_{LR,\Delta p_{TES}}$ of -0.57, while $r_{\alpha,\Delta p_{TES}}$ is limited to 0.27. A high LR causes shorter useful duration both in charge and discharge, as testified by the negative r_{LR,t^*}. The worsening of the TES thermal performance caused by increasing LR, particularly in industrial units, is also highlighted by the increase of the thermocline thickness. High TES aspect ratios provide longer useful durations but at the expense of higher pressure drops. The influence of α over the TES thermal performance in laboratory scaled PBTES is relevant, as shown by r_{α,t^*} higher than 0.6, and compensate for the increased pressure drop. Contrarily, in industrial systems the thermal benefits provided by high aspect ratios are less relevant (r_{α,t^*} of about 0.24). Thus, on the Pareto front α is limited to up to 1. It should be remembered that low aspect ratios imply taller TES units which would suffer from higher stresses on the walls. This might represent a critical roadblock for further upscaling and massive radial flow PBTES installations, unless targeted via a modular approach.

As expected, an increase of the particle size limits the pressure drop but it also causes shorter useful durations. Considering the limited influence of the particle size, it is suggested to act of the LR and aspect ratio (while keeping larger particles in the inner layer and smaller ones in the outer section) to optimize the TES thermodynamic and hydrodynamic performance.

4.3. TES CFD NUMERICAL MODELLING

In terms of CFD modelling, which is the scope of this report, not many cases examine sensible thermal energy storage. In the investigation of Lüle and Asaditaheri [30], a single-tank thermocline storage system filled with solid materials was considered. The discharge process was simulated using the OpenFOAM CFD framework and assuming porous regions within the domain. The numerical mesh consisted of 6000 nodes, the variables of interest were porosity, material sphericity and fluid properties, and the results included streamlines and temperature distributions in the tank. Elfeky et al. [31] performed a numerical investigation that focused on the thermal behaviour of a packed bed TES tank. The unit was a scaled-down model and the aim was to optimize the inlet velocity of the heat transfer fluid (HTF) during the charging/discharging cycles using solid spherical particles as filler materials. The authors approached the modelling using a discrete element method coupled with a CFD solver. Finally, the investigation of Cascetta et al. [32] presents a comparison between CFD and experimental results obtained on a sensible thermal energy storage system based on alumina beads, that were freely poured into a carbon steel tank. The experimental campaign included both the charging and discharging phases. A constant mass flow rate of air was considered. The CFD simulations were carried out using the commercial software FLUENT. The TES domain was modelled using a porous medium approach with the use of appropriate user-defined functions (UDFs). The unsteady Reynolds-Averaged Navier–Stokes (RANS) equations were considered, as well as turbulent effects through the use of the $k-\varepsilon\ RNG$ turbulence model. The numerical domain was a 2D axisymmetric cylindrical tank comprising approximately 30,000 cells and it did not include the solid insulation of the tank.

A comprehensive review of the relevant literature resulted in the formation of the appropriate CFD models that were able to predict a system's response to varying geometries and parameters. The TES zones were treated as porous domains, a choice that is completely justified based on relevant literature. Appropriate equations and properties were implemented as expressions and functions in the model. The complete numerical mesh numbered approximately 340000 cells and could accurately capture the flow. The mesh included the solid insulation volumes around the TES domain and, therefore, wall temperature coupling was not needed. The following paragraphs present the methodology, the numerical results and the concluding remarks of the CFD modelling campaign of the TES unit.

Models and Assumptions

The analysis and evaluation of the TES unit design have been conducted with the use of the commercial CFD software ANSYS Fluent. After the initial evaluation of the modelling options, a two-dimensional, axisymmetric approach was chosen in order to allow for a large number of simulations and the testing of numerous operating set-ups. The pressure-based solver was utilized and a transient formulation was adopted, as the system's dynamic response is of interest in terms of design. Turbulent effects were considered in the inlet and outlet tubes under a RANS framework with the use of the k-ω shear stress transport (SST), while the flow through the thermal storage material has been considered laminar. Gravitational acceleration effects were considered within the TES domain. The compartment filled with thermal storage material has been modeled as a porous zone considering appropriate correlations regarding permeability and porosity and the resulting pressure drop within the unit. More specifically, the Kozeny-Carman equation (**Error! Reference source not found.**) has been considered for the calculation of the pressure drop within the packed bed domain.

$$\frac{\Delta P}{L} = -\frac{180\mu}{\Phi_s^2\, d_p^2}\frac{(1-\varepsilon)^2}{\varepsilon^3}\, u_s \qquad (5)$$

, where ΔP is the pressure gradient, L is the total length of the bed, u_s is the superficial velocity, μ is the viscosity of the working medium, ε is the porosity of the bed, Φ_s is the sphericity of the packed bed particles (assumed value equal to $\Phi_s = 1$ due to the spherical particles of the product Denstone® 2000) and d_s is the diameter of a volume-equivalent spherical particle. A combination of the Kozeny-Carman equation with Darcy's Law (6), yields the correlation for absolute permeability, κ, that has been used in this numerical investigation (7).

$$u_s = -\frac{\kappa}{\mu}\frac{\Delta P}{L} \qquad (6)$$

$$\kappa = \Phi_s^2\,\frac{\varepsilon^3\, d_p^2}{180\,(1-\varepsilon)^2} \qquad (7)$$

Material Properties

The materials that will be used for the construction of the TES unit and are, therefore, of interest for this numerical investigation are presented in Table 4, including their corresponding main properties. Other properties of interest of the used materials are presented in **APPENDIX A**.

TABLE 4. LIST OF MATERIALS/FLUIDS USED FOR THE NUMERICAL ANALYSIS WITH THEIR RESPECTIVE PROPERTIES.

Material / Fluid	Properties			
	Density [kg m^{-3}]	C_p [J kg^{-1} K^{-1}]	k [W m^{-1} K^{-1}]	μ [kg m^{-1} s^{-1}]
Air	*Ideal gas law*	APPENDIX A	APPENDIX A	APPENDIX A

Inconel 625	APPENDIX A	APPENDIX A	APPENDIX A	*N/A*
Denstone® 2000	2180	APPENDIX A	APPENDIX A	*N/A*
Insulation (Layer 1)	128	1130	0.12	*N/A*
Insulation (Layer 2)	114	APPENDIX A	APPENDIX A	*N/A*

Model Validation

To assess and confirm the applicability of the numerical model built in ANSYS Fluent, a relevant validation case has been selected. The examined domain is a thermal energy storage unit comprising the same materials as the designs considered for evaluation. The produced numerical results of the ANSYS Fluent model were compared to available data from KTH, published in [1]. A two-dimensional, axisymmetric domain was created to represent the validation unit, which is presented in Figure 11. The spatial discretisation resulted in a numerical mesh of approximately 335,000 cells. The height of the unit is $L = 0.911\ m$ and its radius is $R = 0.475\ m$. A pressure-based solver was utilised to calculate the flow field. The simulation was transient, with the time step (dt) set to $dt\ = 1\ s$. The overall simulated time was 14,400 seconds or 4 hours. Turbulent effects were considered in the inlet and outlet tubes under a RANS framework with the use of the k-ω shear stress transport (SST), while the flow through the thermal storage material has been considered laminar. Gravitational acceleration effects were considered within the TES domain. Air was the working medium of the simulation and was modelled as an ideal gas. The thermal storage zone has been modelled as a porous zone considering appropriate correlations regarding permeability and porosity. The boundary conditions of the validation case are presented in Table 5.

TABLE 5. BOUNDARY CONDITION TYPES AND VALUES FOR THE VALIDATION CASE.

Boundary Condition	Type	Value
Inlet Mass Flow :	Constant value	0.0287 kg s-1
Inlet Temperature:	Variable	200 to 800 °C
Outlet Pressure:	Constant value	101325 Pa

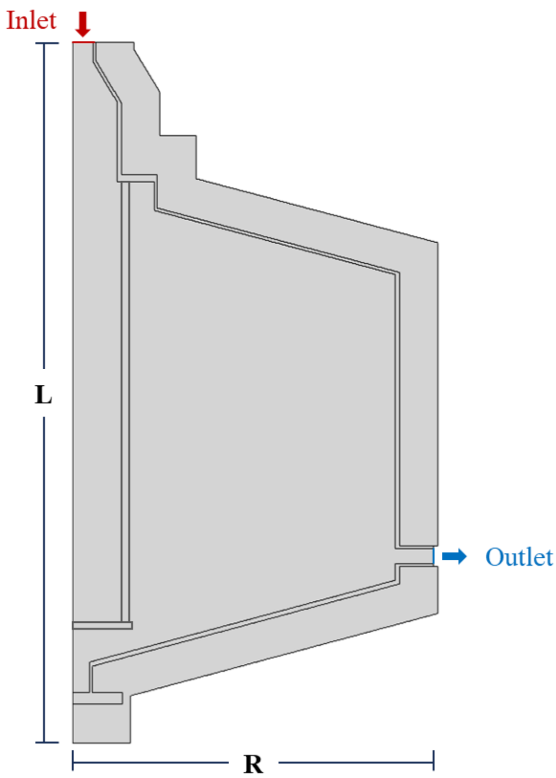

FIGURE 11. AXISYMMETRIC NUMERICAL DOMAIN OF THE THERMAL ENERGY STORAGE UNIT USED FOR VALIDATION PURPOSES.

The results of the validation simulation were evaluated in terms of the TES unit outlet average temperature and compared to data from the KTH investigation. The data comparison is presented in Figure 12.

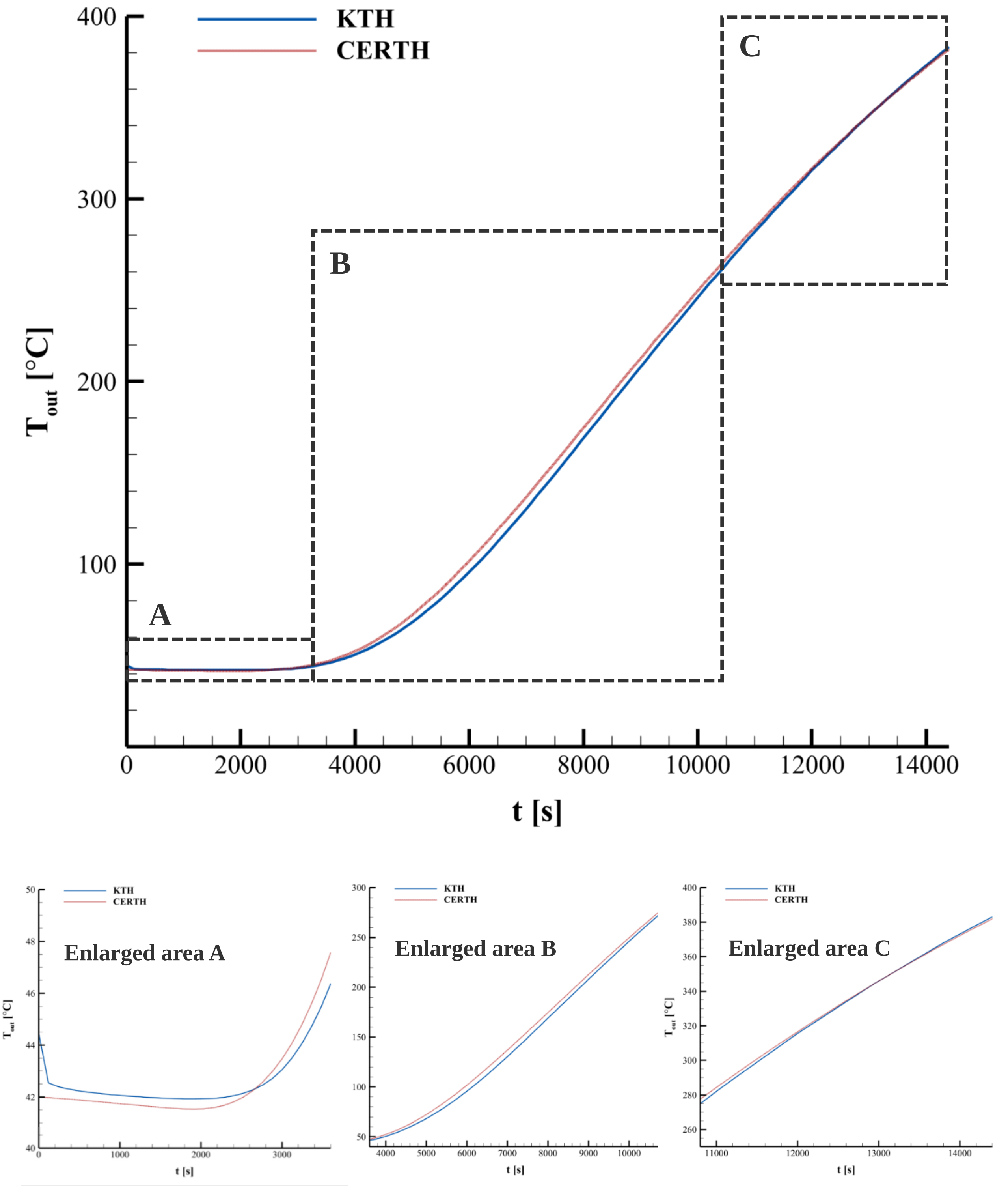

FIGURE 12. EVOLUTION OF OUTLET AVERAGE TEMPERATURE OVER A PERIOD OF FOUR HOURS. DATA COMPARISON BETWEEN KTH AND CERTH RESULTS FOR MODEL VALIDATION PURPOSES. ENLARGED AREAS A, B AND C ARE PRESENTED AT THE BOTTOM OF THE FIGURE.

4.4. TES CFD PERFORMANCE RESULTS

The final goal of the present investigation is to assess a number of proposed TES unit designs (different geometries), based on the developed numerical model. Four different configurations are proposed. They are the final "candidates" based on KTH's laboratory experience and research and differ in terms of the outlet tube configuration. The geometries are presented in Figure 13. The main variables that need to be defined are the TES pressure drop, the unit's thermal storage capacity which will be evaluated by comparing the average outlet temperature of each design and the presence of any recirculation zones that may affect the uniformity of the thermal storage capacity of the unit. The results of this investigation are presented in this paragraph.

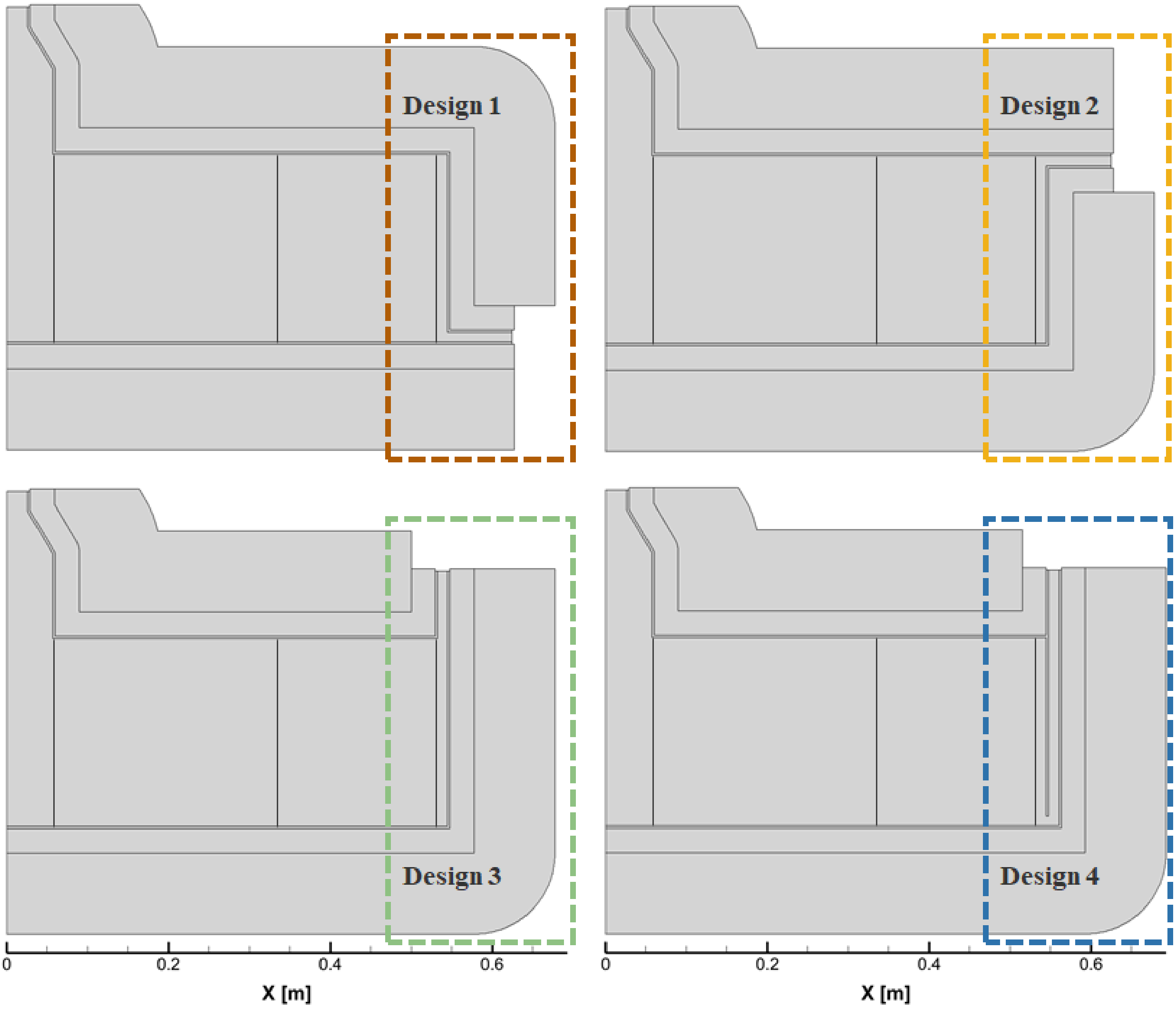

FIGURE 13. THERMAL ENERGY STORAGE UNIT DESIGNS TO BE EVALUATED

Initial, Boundary Conditions and Parameters of Interest

The present paragraph summarises the main conditions and parameters that govern the numerical analysis performed. The materials considered, have been presented in the methodology section. The thermal energy storage (TES) units were represented as two-dimensional, axisymmetric domains. The spatial discretisation resulted in a numerical mesh of approximately 340,000 cells. The height of the unit is $H = 0.549\ m$ and its radius is $R = 0.678\ m$. A pressure-based solver was used for the flow calculations. The simulation was transient, with the time step (dt) set to $dt\ = \ 1\ s$. The overall simulated time was 14,400 seconds or 4 hours. Turbulent effects were considered in the inlet and outlet tubes under a RANS framework with the use of the k-ω shear stress transport (SST), while the flow through the thermal storage material has been considered laminar. Gravitational acceleration effects were considered within the TES domain. Air was the working medium of the simulation and was modelled as an ideal gas. The thermal storage zone has been modelled as a porous zone considering appropriate correlations regarding permeability and porosity that have been reported in the methodology section. Finally, the main initialisation values are mentioned in Table 6, the boundary conditions of the system are presented in Table 7 and a list of parameters of interest that have been further investigated is included in Table 8.

TABLE 6. INITIAL CONDITIONS FOR THE NUMERICAL ANALYSIS OF THE TES SYSTEM DESIGNS.

Initial Condition	Type	Value
Domain pressure	Constant value	$101325\ Pa$
Domain temperature	Constant value	$200\ °C$
Domain velocity	Constant value	$U_x\ =\ U_y\ =\ 0\ m/s$

TABLE 7. BOUNDARY CONDITION TYPES AND VALUES FOR THE NUMERICAL ANALYSIS OF THE TES SYSTEM DESIGNS.

Boundary Condition	Type	Value
Inlet Mass Flow	Constant value	$0.0287\ kg/s$
Inlet Temperature	Constant value	$800\ °C$
Outlet Pressure	Constant value	$101325\ Pa$

TABLE 8. VARIABLES OF INTEREST USED FOR PARAMETRIC INVESTIGATION.

Parameter	Main / nominal value	All examined values
Separator location	$344\ mm$	$135, 163, 218, 344\ mm$
Particle diameter	$5\ mm$	$5, 10, 20\ mm$
Porosity	$0.38\ [-]$	$0.38, 0.42\ [-]$
Mass flow rate	$27.4\ g/s$	$27.4, 54.7\ g/s$

Design Evaluation

This paragraph presents the results of the numerical analysis of the four TES designs in a comparative manner. The evolution of the temperature value at the outlet of the TES units over a charge period of 4 hours and an equivalent discharge period is presented in Figure 14. The results suggest that designs 1,2 and 3 exhibit similar behaviour in terms of the outlet temperature of the working medium. Design 4, however, due to the extended pathway downstream of the thermal storage area, results in a mild differentiation of the outlet temperature profile, especially during the discharge phase.

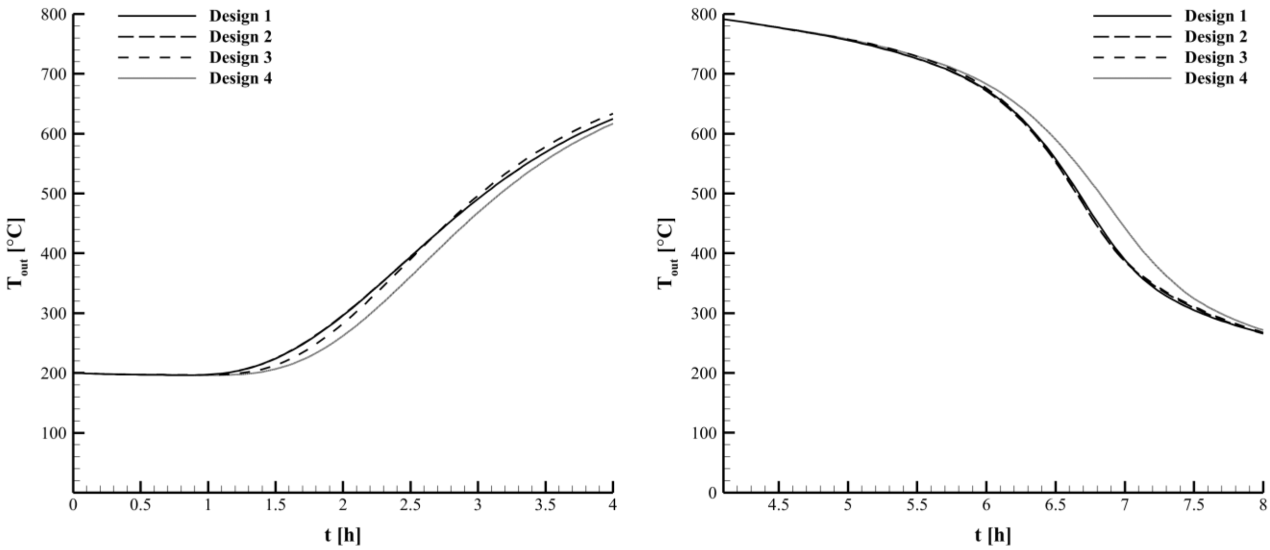

FIGURE 14. TEMPERATURE VALUE AT THE OUTLET OF THE EXAMINED TES UNITS. DATA CORRESPOND TO A PERIOD OF FOUR HOURS, DURING THE CHARGING PHASE (LEFT) AND TO A PERIOD OF FOUR HOURS, DURING THE DISCHARGING PHASE (RIGHT).

As the charging phase proceeds, the temperature of the TES materials increases. To quantify the effect of the TES design on the unit's charging capability, the average temperature of the thermal storage material i.e. Denstone ® 2000, is plotted in Figure 15 for a 4-hour charging and equivalent discharging period.

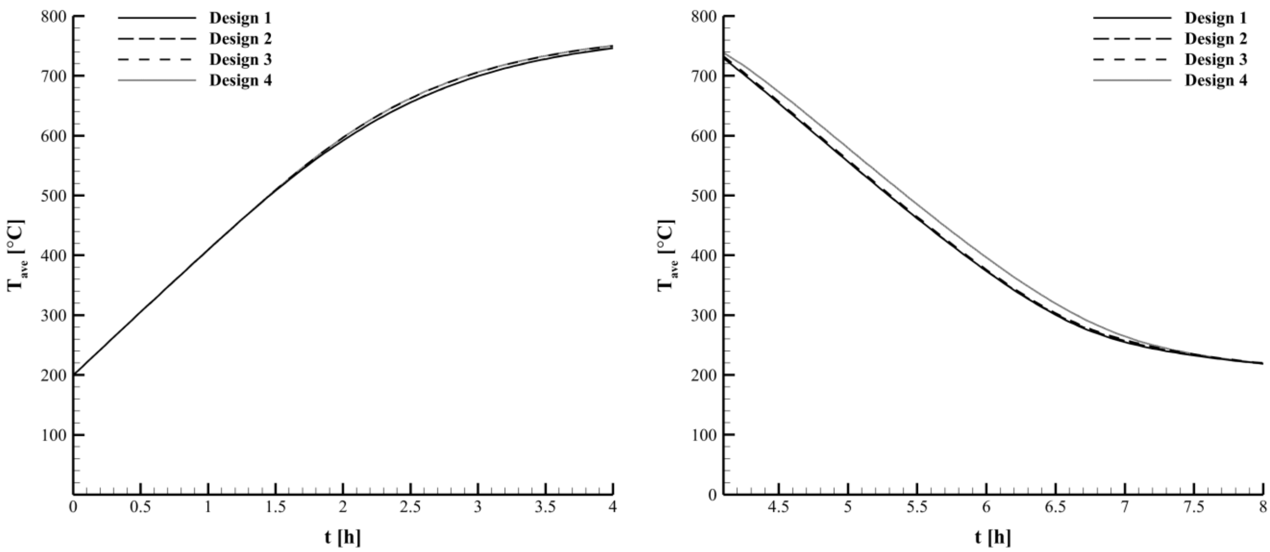

FIGURE 15. AVERAGE TEMPERATURE WITHIN THE VOLUME OF THE THERMAL STORAGE MATERIALS. DATA CORRESPOND TO A PERIOD OF FOUR HOURS, DURING THE CHARGING PHASE (LEFT) AND TO A PERIOD OF FOUR HOURS, DURING THE DISCHARGING PHASE (RIGHT).

The temperature distribution within the four TES designs is depicted in Figure 16. The comparative contours show the TES temperature at time, $t = 4\ hours$ after the initialisation of the charging phase. The simulation results are comparable for all four designs, without revealing disadvantages for a specific geometry. The thermal load is distributed evenly within the thermal storage material and the layers encapsulating the unit, provide adequate thermal insulation.

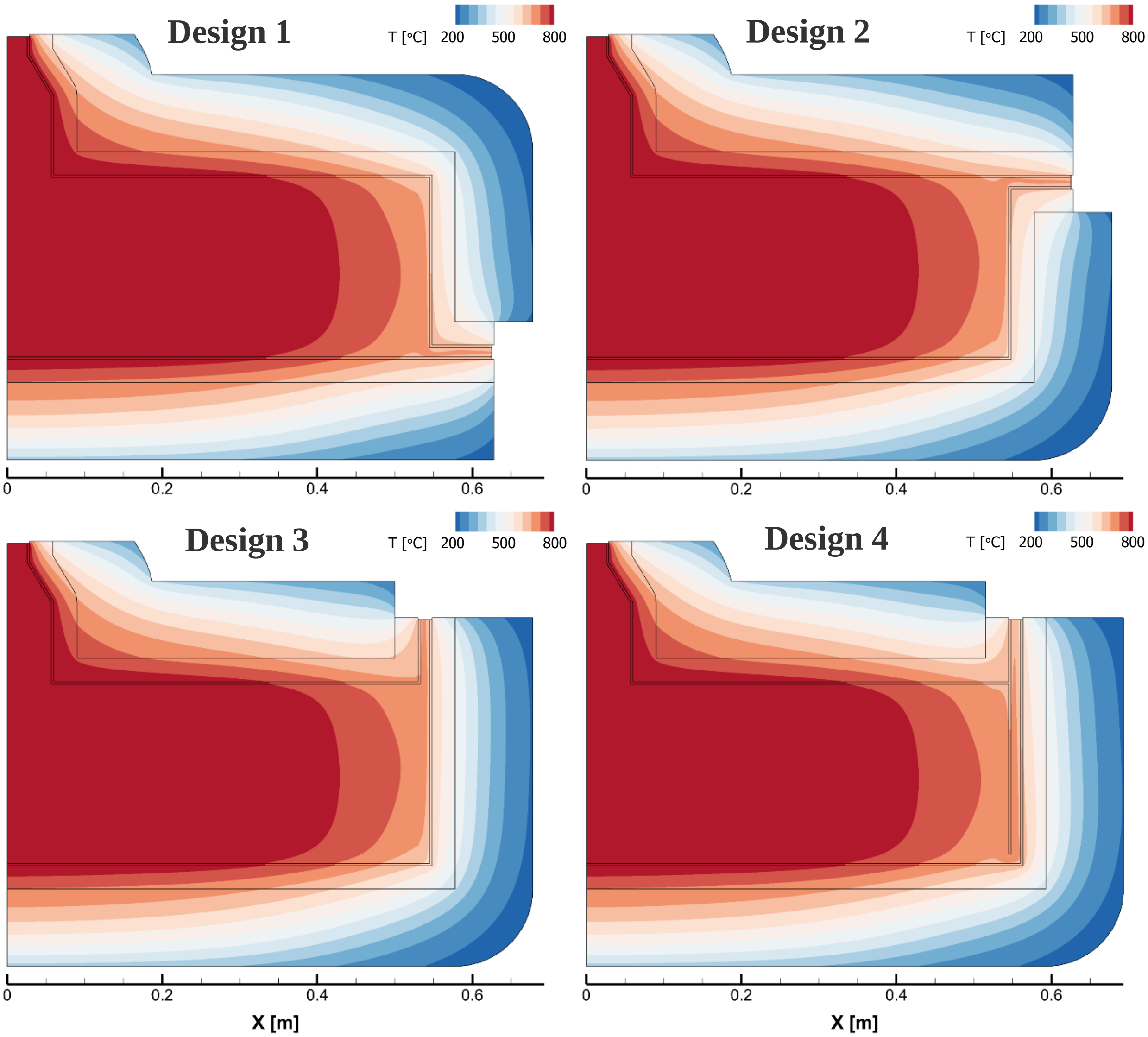

FIGURE 16. CONTOUR PLOT OF TEMPERATURE FOR DESIGNS 1 TO 4 FOR TIME, T=14400 S. TEMPERATURE DISTRIBUTION ON THE INSULATION LAYERS IS INCLUDED.

Pressure drop in the TES unit is an important design parameter and is presented in Figure 17. More specifically, the pressure difference between the inlet and the outlet is plotted for the four designs during both the charging and discharging phases. Again, apart from the differentiation of "Design 4" due to the geometrical reasons that were already mentioned, the remaining geometries exhibit similar pressure-drop behaviour. The similarities of the four designs in terms of resulting temperature fields and pressure drop imply that, for the assigned mass flow rate of air, the flow within the porous thermal storage domain remains relatively uniform, regardless of the outlet configuration. This assumption was corroborated by visualising the flow path lines within the four domains as presented in Figure 18, where the outlet opening imposes minor flow changes, limited only to the final part of the thermal storage volume. The path lines of the flow are coloured by the magnitude of the flow velocity.

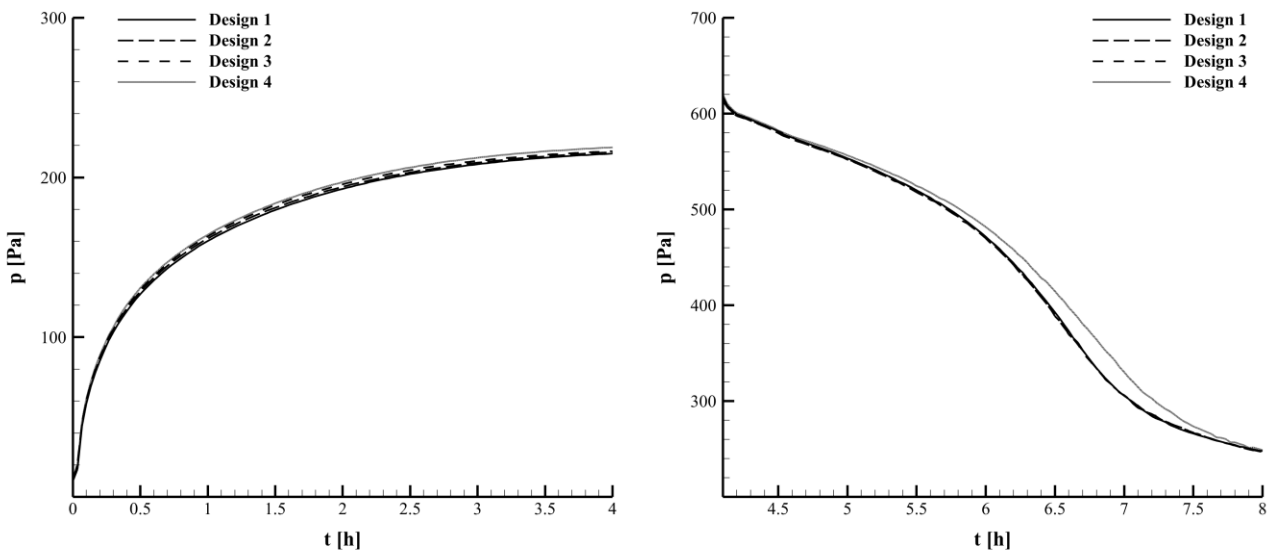

FIGURE 17. PRESSURE DIFFERENCE BETWEEN THE INLET AND OUTLET OF THE FOUR TES DESIGNS. DATA CORRESPOND TO A FOUR-HOUR CHARGING PERIOD (LEFT) AND AN EQUIVALENT DISCHARGING PERIOD (RIGHT).

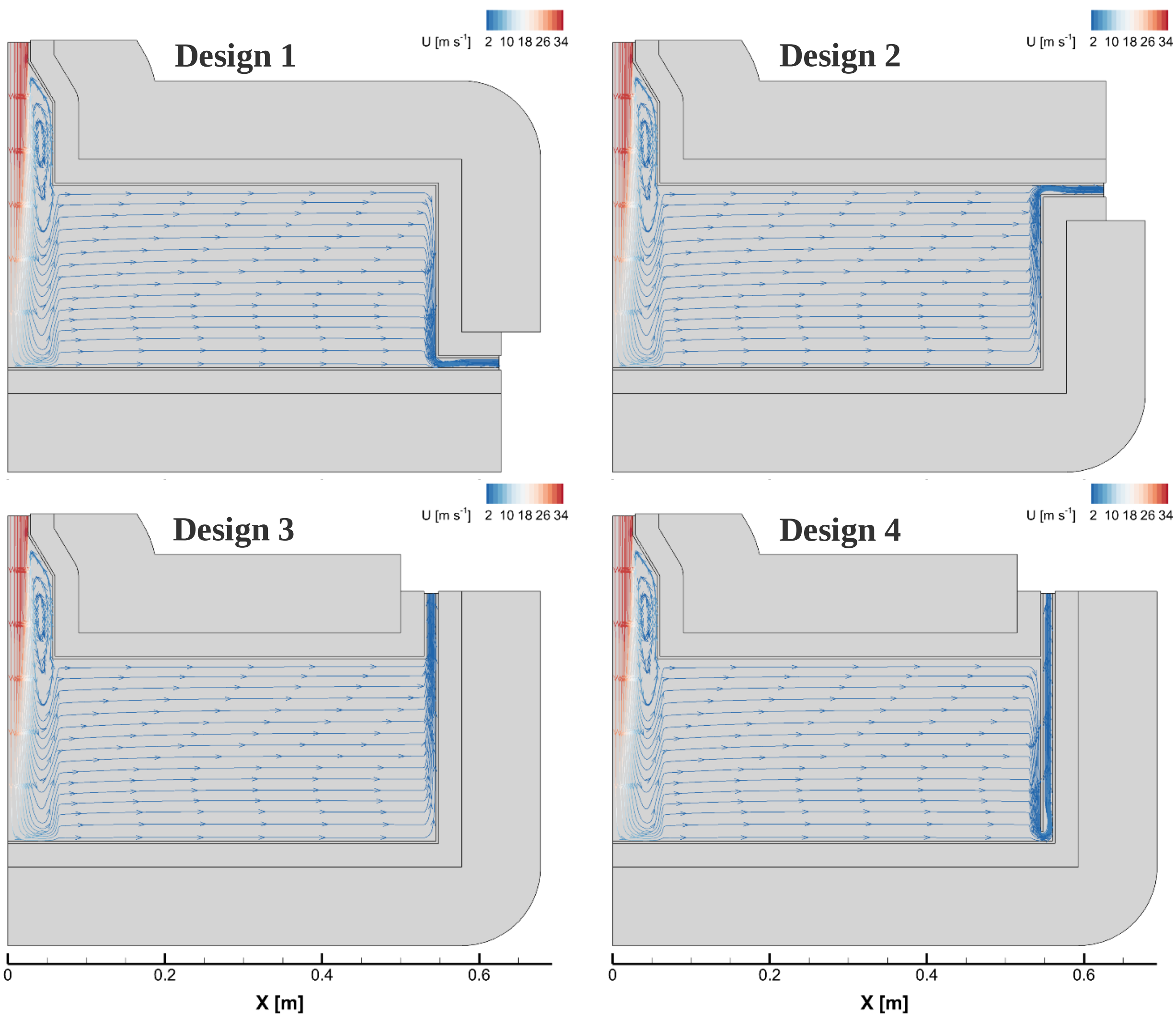

FIGURE 18. FLOW PATH LINES FOR THE FOUR EVALUATED TES DESIGNS. LINES CLOURED BY VELOCITY MAGNITUDE

Parametric Investigation

The results from the evaluation of the four TES designs revealed minor differences in terms of TES capacity and efficiency. In terms of manufacturing, designs 1,2, and 3 have a small advantage over design 4 due to the absence of the folding outlet tube and, finally, design 3 provides an advantage in terms of ease of operation and connectivity due to the fact that inlet and outlet height levels are closer than the other designs. Therefore, design 3 was selected for analysing the sensitivity of the TES system to the following parameters:

- ### Separator location

The separator is a cylindrical wireframe that is placed within the TES unit and separates "Domain 1" from "Domain 2" in order to fill the unit with material of different particle diameters. The investigation that was presented in the previous paragraph assumed that the length, L, of the radius at which the separator is placed was 344 mm and the respective domain can be examined in Figure 19. To evaluate the effect that the separator location has on the pressure drop and the average temperature of the TES system, three more separator locations were examined, namely at 135 mm, 163 mm and 218 mm, and the results are presented in Figure 20.

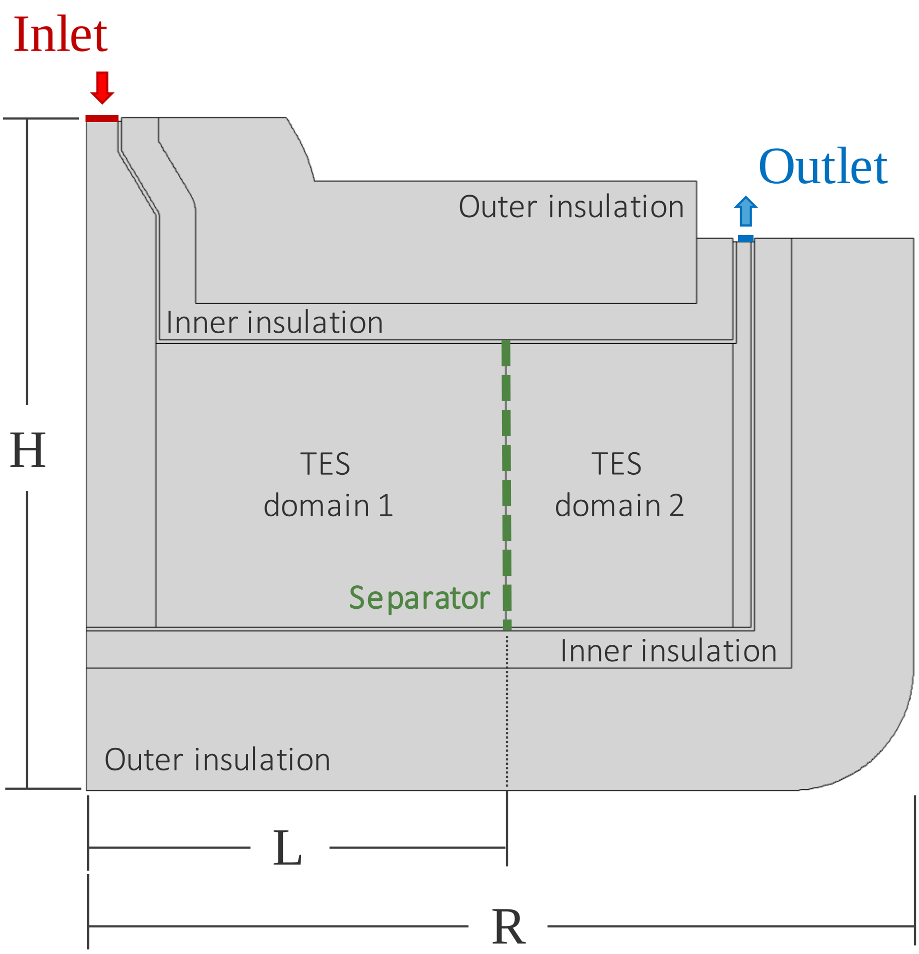

FIGURE 19. SEPARATOR POSITIONING WITHIN THE TES DOMAIN

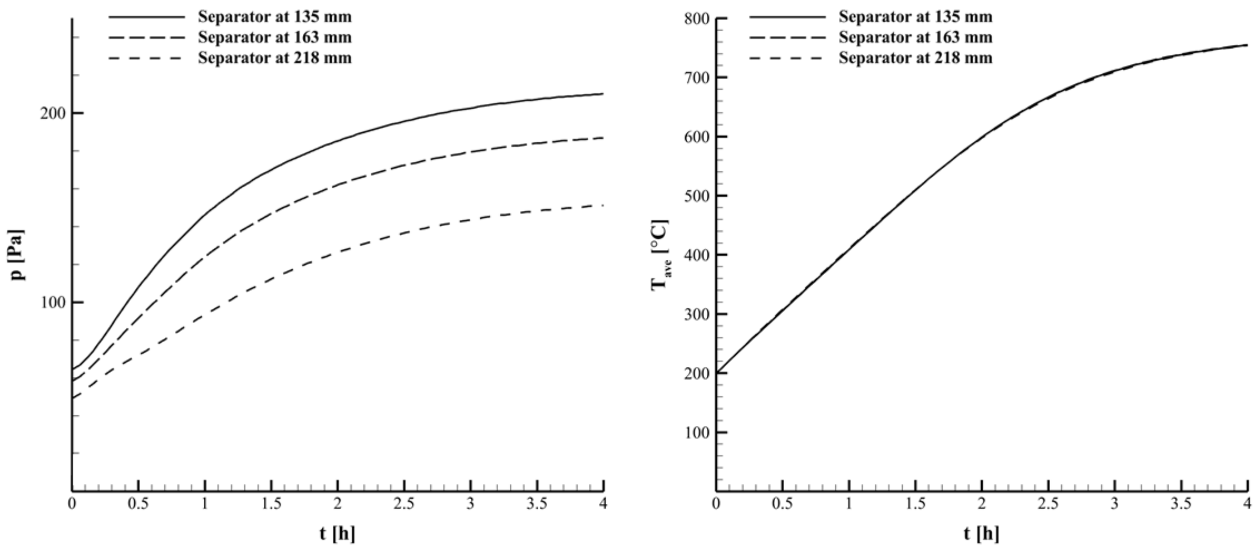

FIGURE 20. PRESSURE DROP AND OUTLET TEMPERATURE OF THE TES SYSTEM FOR A CHARGING PERIOD OF FOUR HOURS IN THE CASE OF DIFFERENT SEPARATOR POSITIONS.

- Thermal storage particles' diameter

The use of thermal storage materials of different particle diameters can positively affect the system in terms of pressure drop. In this section, an investigation of four particle size combinations has taken place. The location of the separator is fixed and set to $L = 163\ mm$. The topology of the system can be examined in Figure 21. The particle size (d_{p_1}) within "Domain 1" is set to 5, 10 and 20 mm while the particle size (d_{p_2}) within "Domain 2" is set to 5 and 10 mm. The plots of pressure drop and average temperature evolution within the thermal storage volume resulting from the four different particle size combinations are presented in Figure 22.

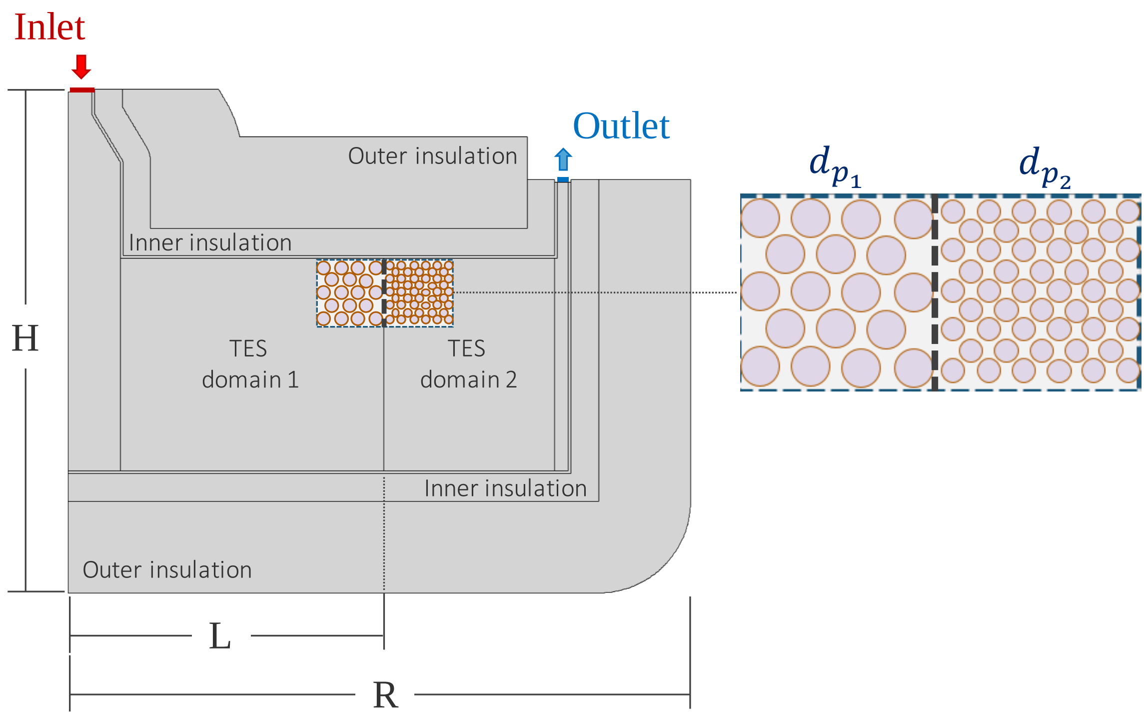

FIGURE 21. TOPOLOGY OF TES SYSTEM DOMAINS OF DIFFERENT PARTICLE SIZES.

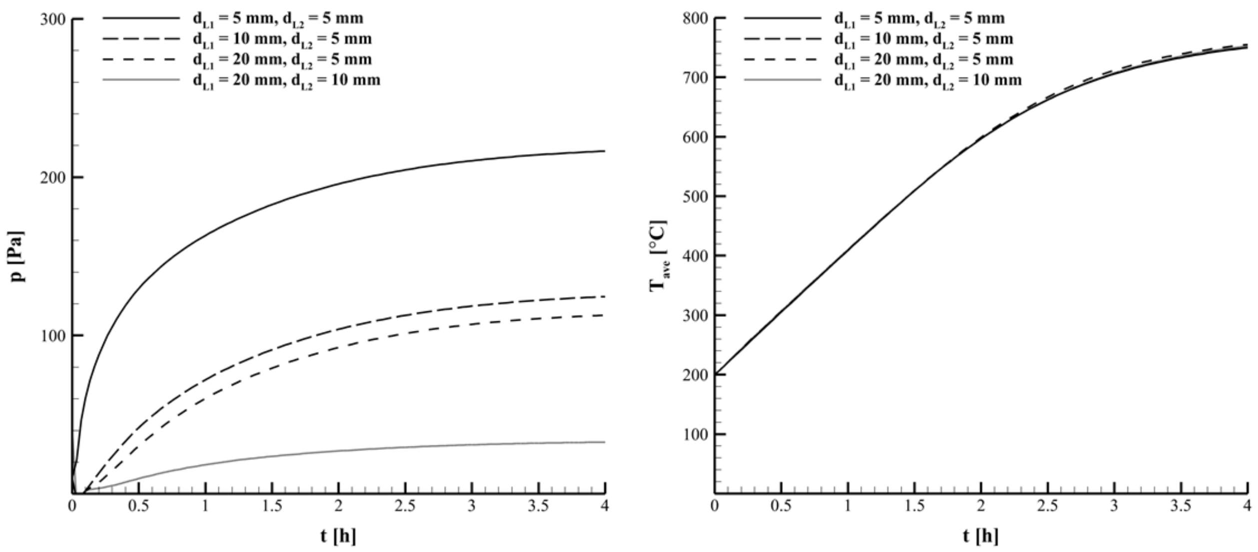

FIGURE 22. PRESSURE DROP AND OUTLET TEMPERATURE OF THE TES SYSTEM FOR A CHARGING PERIOD OF FOUR HOURS IN THE CASE OF DIFFERENT PARTICLE SIZE COMBINATIONS.

- ## Porosity variation

The porosity that is normal to be expected within the TES unit, according to the material manufacturer is approximately 0.38. In the case of problematic material placement or deviations from the nominal values, the porosity is expected to increase, up to a value of 0.42. An investigation of the system's response to the mentioned porosity values was performed and the results, regarding pressure drop and average system temperature during a four-hour period, are presented in Figure 23.

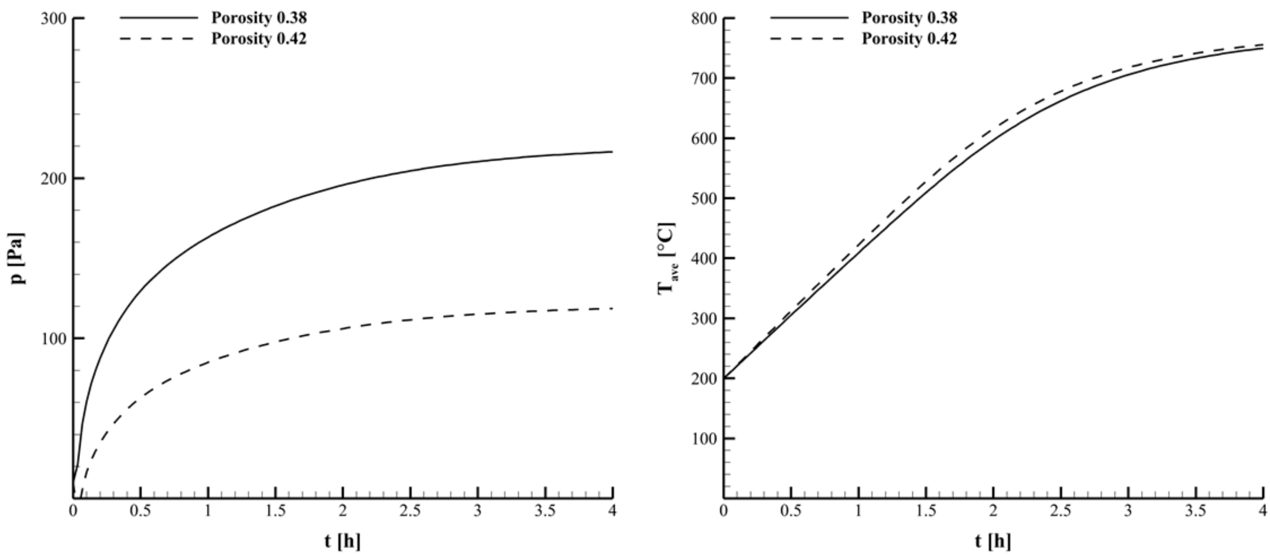

FIGURE 23. PRESSURE DROP AND OUTLET TEMPERATURE OF THE TES SYSTEM FOR A CHARGING PERIOD OF FOUR HOURS, FOR TWO POROSITY VALUES.

- Mass flow rate variation

Finally, the response of the system to a variation in the expected flow rate was examined. Except for the nominal mass flow rate of $28.7\ g/s$, two scenarios, one of a mass flow rate of double the value, i.e. $57.4\ g/s$ and one of half the nominal value, i.e. $14.35\ g/s$, were investigated. The pressure drop evolution and the average temperature during a four-hour period, have been included in Figure 24.

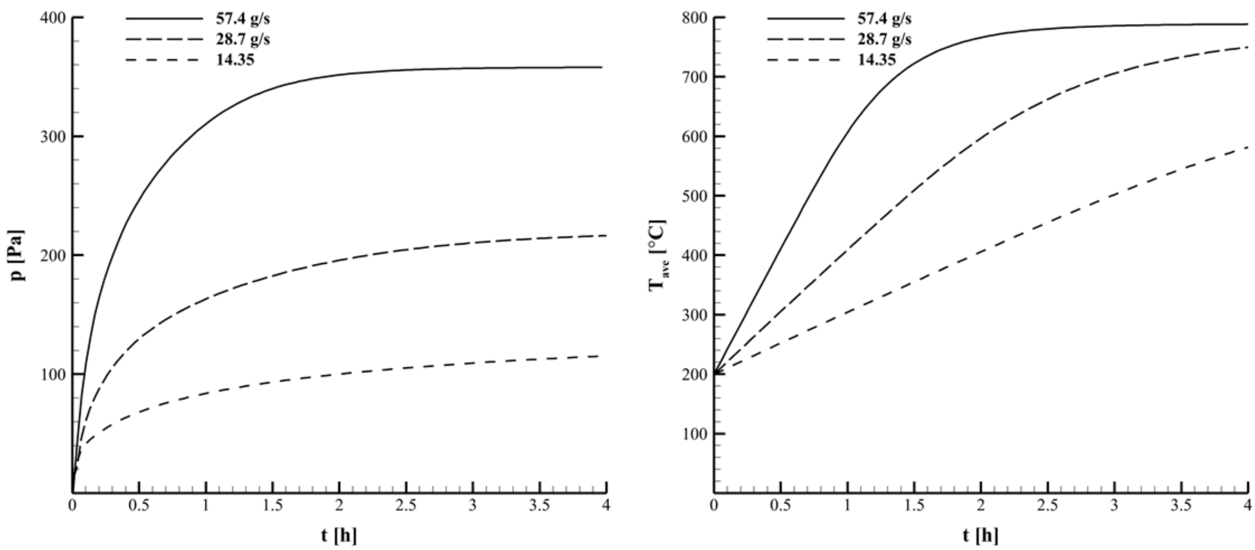

FIGURE 24. PRESSURE DROP AND OUTLET TEMPERATURE OF THE TES SYSTEM FOR A CHARGING PERIOD OF FOUR HOURS, FOR TWO MASS FLOW RATES.

4.5. NUMBER OF OUTLETS ANALYSIS

Another aspect of the PBTES design that was analyzed was the influence of the number of outlets in the thermodynamic performance. More specifically, a 2D CFD model was developed using FEM, aiming at investigating the flow and heat distribution during charging and discharging along the horizontal direction of the TES. The geometries used in the model and shown in Figure 26, represented 1/8 (4 outlets) and 1/12 (6 outlets) of the total horizontal cross-sectional area of the TES, assuming that the flow distribution is symmetric in the radial directions. The influence of having a circular annulus around the main bed was also investigated for the 4 and 6 outlet scenarios in similar CFD simulations, by removing the fluid domains (annulus) shown in Figure 26. The simulations were performed assuming:

- a temperature range of 200 and 800 °C between the hot and cold air.
- a charging/discharging power of 20/10 kW respectively.
- Uniform inflow along the inlet curve for charging.
- Uniform inflow along the outlet curve for discharging.
- Symmetry conditions in the side walls.
- Convective heat transfer along the outer wall.

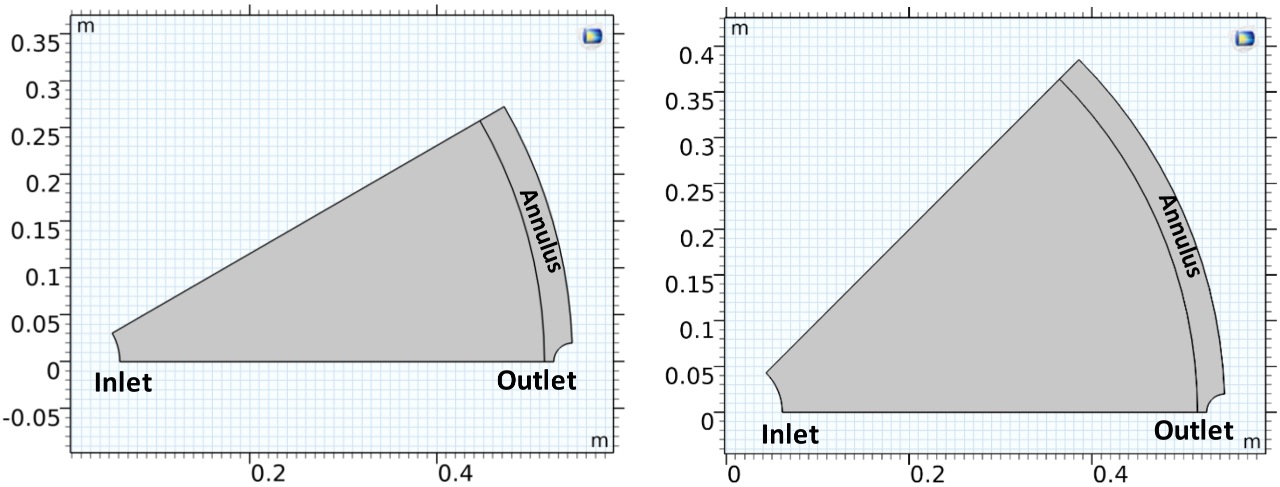

FIGURE 26: GEOMETRIES USED FOR 'NUMBER OF OUTLETS' ANALYSIS

As illustrated in Figure 25, the number of outlets seems to have minimal impact on the outlet temperature during charging or discharging when an outer fluid domain (annulus) is considered. In the scenarios without any annulus, the total energy capacity of the system is increased by approximately 12% since there is more available volume for the PB, but the outlet temperature is strongly affected, especially during discharging. The thermocline development along the bed was quite similar in the annulus and no-annulus scenarios for the charging process, but the discharging results indicate that the existence of the annulus helps distribute the flow uniformly along the bed. In the no-annulus scenario, the thermocline expands faster and outside the radial direction, resulting in reduced outlet temperatures, early in the discharge phase. Another notable result is that in the no-annulus scenario, the existence of 4 and 6 outlets produces significantly different results, showing that the addition of more outlets improves the flow distribution for both charging and discharging. The pressure drop profiles were similar for all 4 cases, but slightly increased pressure drops were observed for the no-annulus cases. Overall, the existence of the annulus is considered beneficial for the operation of the PBTES while the two extra outlets are not improving the performance and thus, are not required.

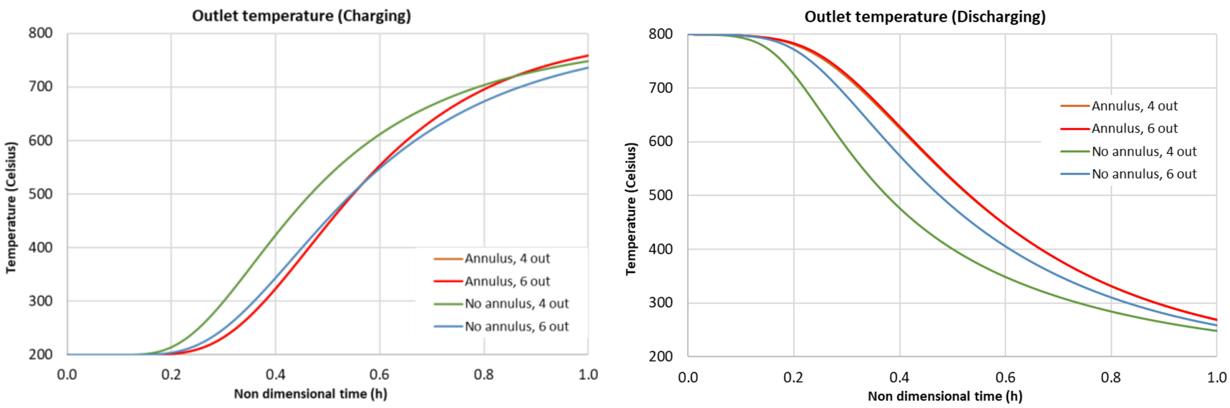

FIGURE 25: OUTLET TEMPERATURE PROFILES FOR CHARGING AND DISCHARGING SIMULATIONS OF THE 4 GEOMETRIES

4.6. THERMOMECHANICAL ANALYSIS

The thermomechanical performance of the PBTES was also assessed for the innovative PBTES concept proposed, using 2D and 3D FEM analysis. The model developed has aimed at investigating the effects of thermal expansion on the PBTES tank, ensuring structural stability in the operating temperature range. Initially, axisymmetric 2D simulations have been performed considering the simplified geometry shown in FIGURE 27. The mesh elements are quadratic axisymmetric, with an average size of 2 mm, .

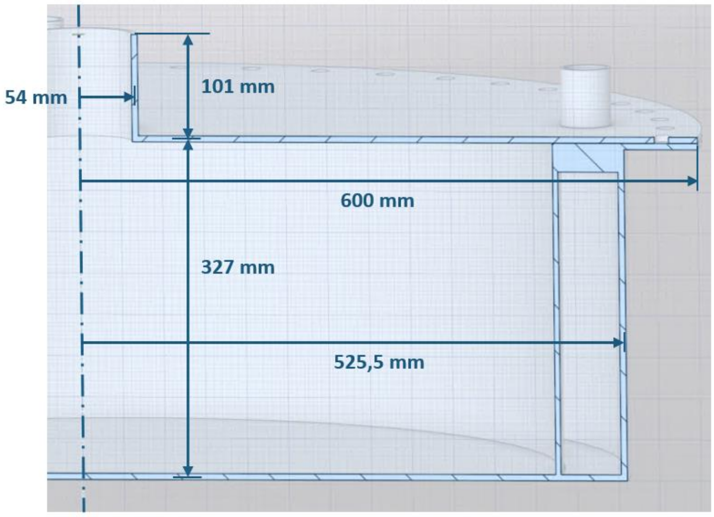

FIGURE 27: SIMPLIFIED 2D GEOMETRY (WALL THICKNESS 6MM)

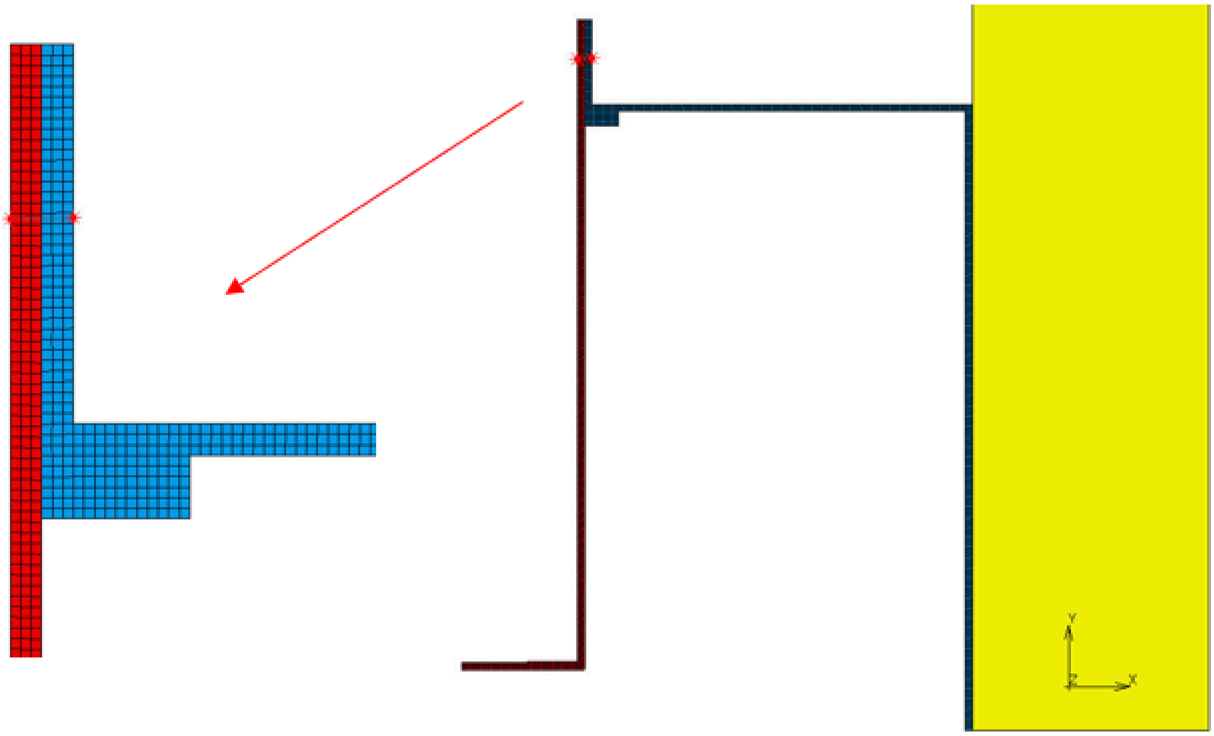

FIGURE 28: MESH DETAIL

Stainless steel 1.4835 (AISI 253MA) was used, the material description also takes into account the temperature effect on mechanical properties and on plastic field of the stress-strain relation (also with temperature dependance).

The TES is not physically constrained; it is simply placed on the ground. Therefore, a contact must be used to model the interaction between a meshed deformable body (the TES) and a rigid one (the ground, not meshed, represented geometrically only).

Regarding mechanical boundaries, contacts were also used to model the interaction between the body of the TES and its cover, which are constrained together with a bolted joint. This joint is modeled in the F.E.M. as a mono-dimensional element with pre-load (M18 – thickness 18 mm and preload 92kN). Friction is also considered, with μ = 0.7 (steel-steel) and μ = 0.2 (steel-concrete) as friction coefficients.

Thermal constraints are the most important conditions applied for this analysis. The initial temperature is 20°C (293K). The operative temperatures were derived from CFD results (as from section 4.3 and as shown in Figure 30), thus, timetables impose the temperature distribution (in X-Y). Following the CFD results, two cycles were analyzed in the thermo-mechanical Finite Element Model: 4 hours charge and 4 hours discharge, with time steps every 30 minutes. During the first cycle, temperature raises up to around 800°C in hot spots, before decreasing in the second cycle. Although the TES is not physically constrained, gravity is acting on it, so the own weight of the metal is subject to this effect. The internal particulate mass is not modeled, instead its weight is accounted with a pressure acting on lower plate of the TES (P = 8000 N/m2).

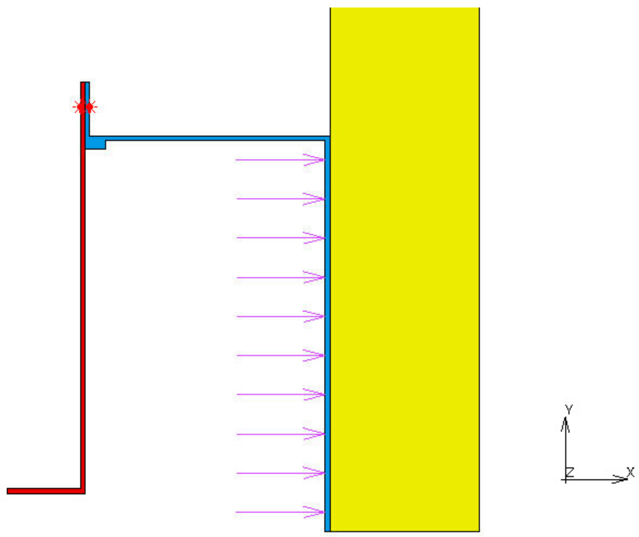

FIGURE 29 - MECHANICAL BOUNDARIES

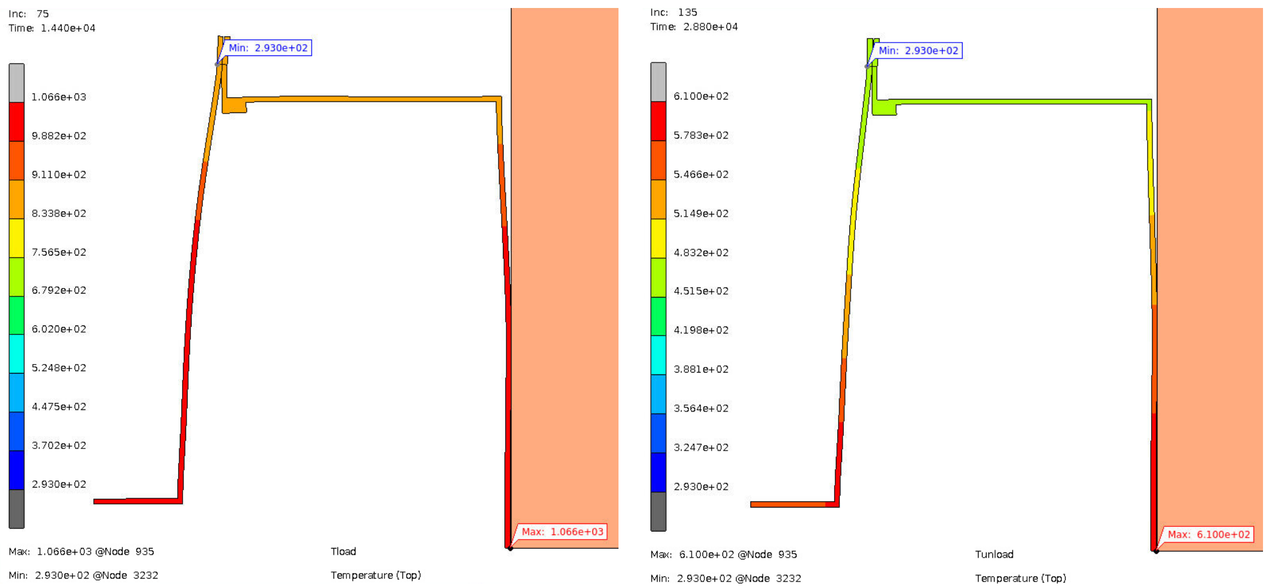

(a) (b)

FIGURE 30: ASSUMED TEMPERATURE DISTRIBUTION AFTER 4 HOURS OF CHARGING (A) AND 4 HOURS OF DISCHARGING (B). TES DEFORMATION DIRECTLY SHOWN IN THE DRAWINGS (SCALE 1:1)

The preliminary results showed potentially relevant deformation at both the bottom and top side of the TES due to thermal expansion; thus, demanding a more detailed 3D examination for the TES prototype. Relevant stresses are also recoded, however, they are within the boundaries imposed by the selected materials. The most critical area is represented by the bolted joint. These specific results highlight the need for more detailed analysis focused on upscaled TES units and their thermal stresses and deformations coupled with detailed considerations on the materials for the TES structure. This specific work on upscaled unit is currently planned in the context of the second part of WP4 ensuring a further derisking of the solution.

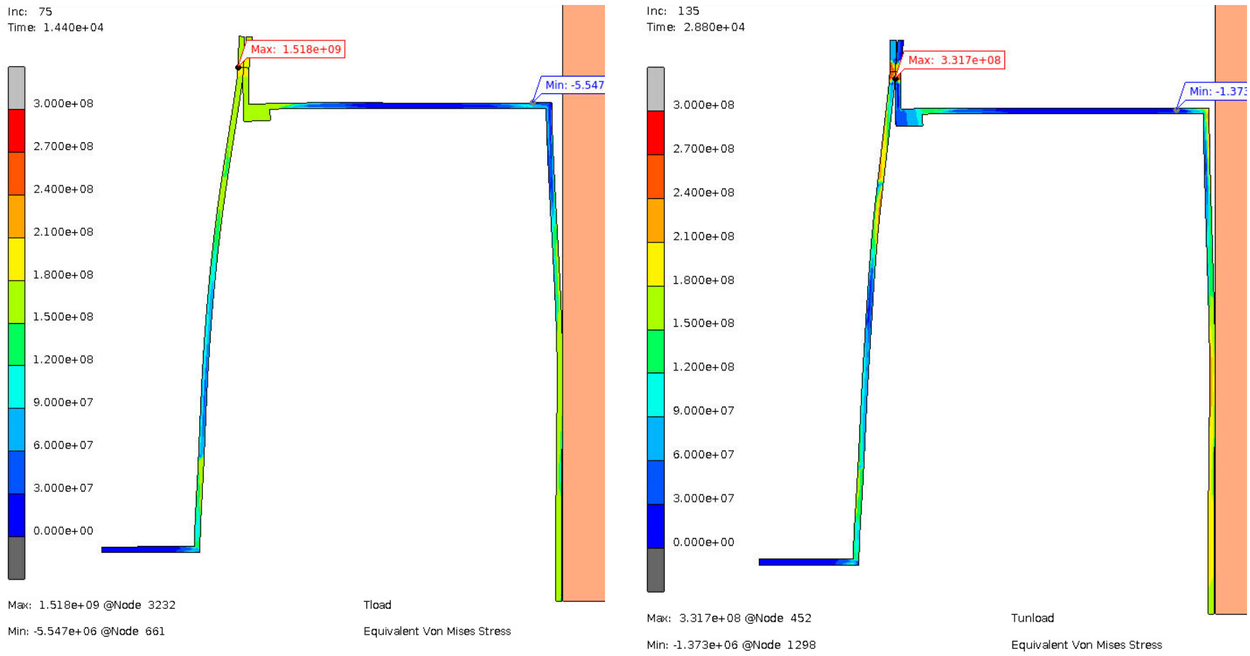

(a) (b)

Figure 31: Equivalent Von Mises stresses after 4 hours of charging (a) and 4 hours of discharging (b). TES deformation directly shown in the drawings (scale 1:1)

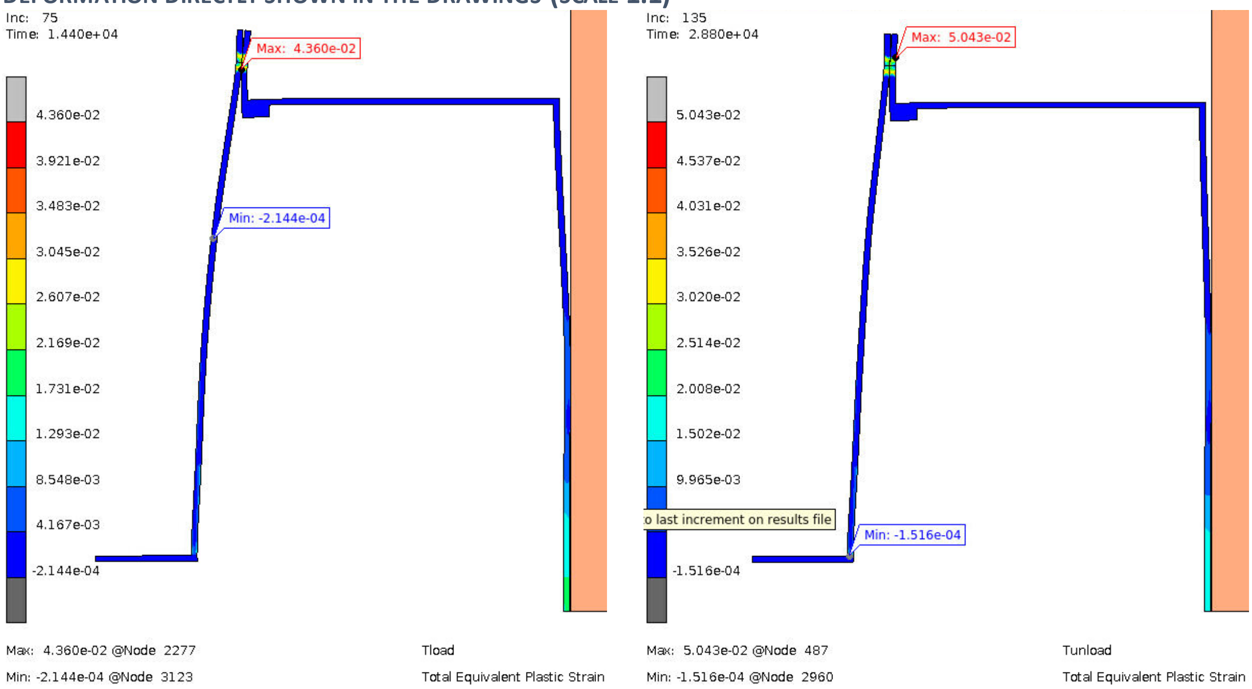

(a) (b)

Figure 32: Total equivalent plastic strain after 4 hours of charging (a) and 4 hours of discharging (b). TES deformation directly shown in the drawings (scale 1:1)

For a deeper assessment a 3D model was developed. The geometry was split on 4 identical and symmetric parts in order to reduce the simulation time requirements and the general form of the PDEs solved is: (1) General form of the Cauchy momentum equation, (2) Heat equation, (3) Fourier's law for conductive heat transfer.

$$\rho a_f = \nabla * \sigma + F_V \; (1)$$

$$\rho C_p u * \nabla T + \nabla * \mathrm{q} = \mathrm{Q} + Q_{ted} \; (2)$$

$$\mathrm{q} = -\mathrm{k}\nabla\mathrm{T} \; (3)$$

To simplify the simulation process, the thermal part is simulated by applying an expected thermal front to all domains, without solving simultaneously the fluid flow and convective heat transfer equations in the same simulations. The material properties considered for the simulation are the same for all parts of the geometry and they correspond to high-temperature stainless steel (253MA), which is expected to be also the material for the experimental TES rig.

Different boundary conditions are applied to the domains in order to simulate a representative operation for the system:

- The bottom area of the TES is restricted to moving on the z direction.
- Gravity is considered in all parts of the domains.
- The weight of the solid filler particles is considered as a boundary load applied to the bottom of the TES tank.
- The internal and external pressure applied to all inner and outer walls respectively as a boundary load.
- The thermal front applied is a function of the radial distance from the center of the tank (inlet) which is assumed to have a maximum temperature of 800 °C. The minimum temperature is found on the outer side of the outer tank walls, and it's approximately 500 °C.
- Symmetry boundary conditions are considered along the cross-sections in the z-x and z-y planes, since 1/4 of the full geometry is used.

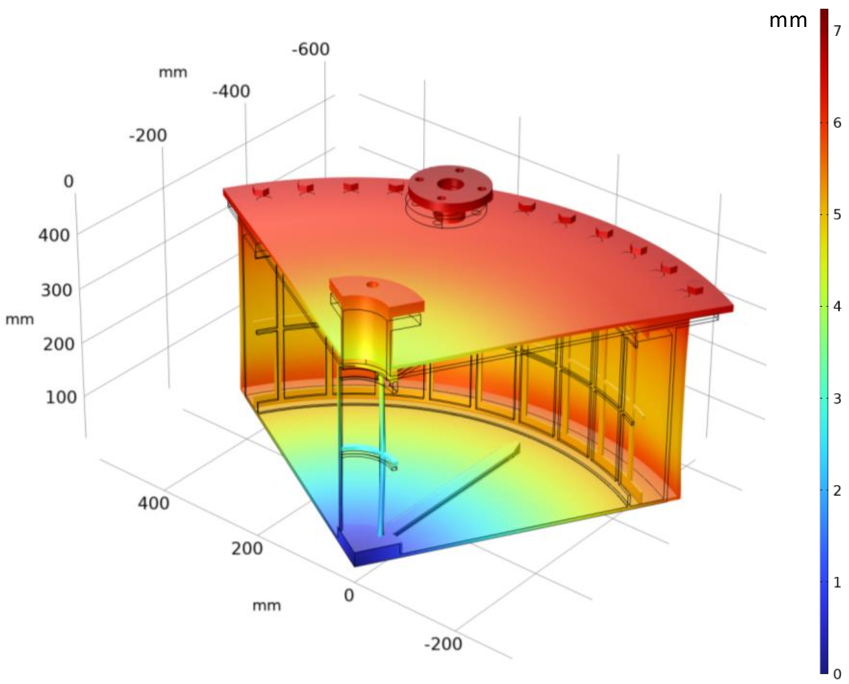

FIGURE 33: DISPLACEMENT MAGNITUDE RESULTS FOR THE OPERATION OF THE PBTES, UP TO 800 C. 1/4 OF THE FULL TANK IS DISPLAYED

Simulation results are illustrated in Figure 33 and indicate that the thermal expansion is not significant and remains restricted to values below 7 mm. The tank is expanding outwards in all directions which results in increased stresses at the wall connection points. The maximum amount of displacement is found around the perimeter of the tank's top lid, while the maximum stresses are expected around the inlet pipe in the centre of the tank, as well as at the connection points between the side walls and the bottom area of the PBTES.

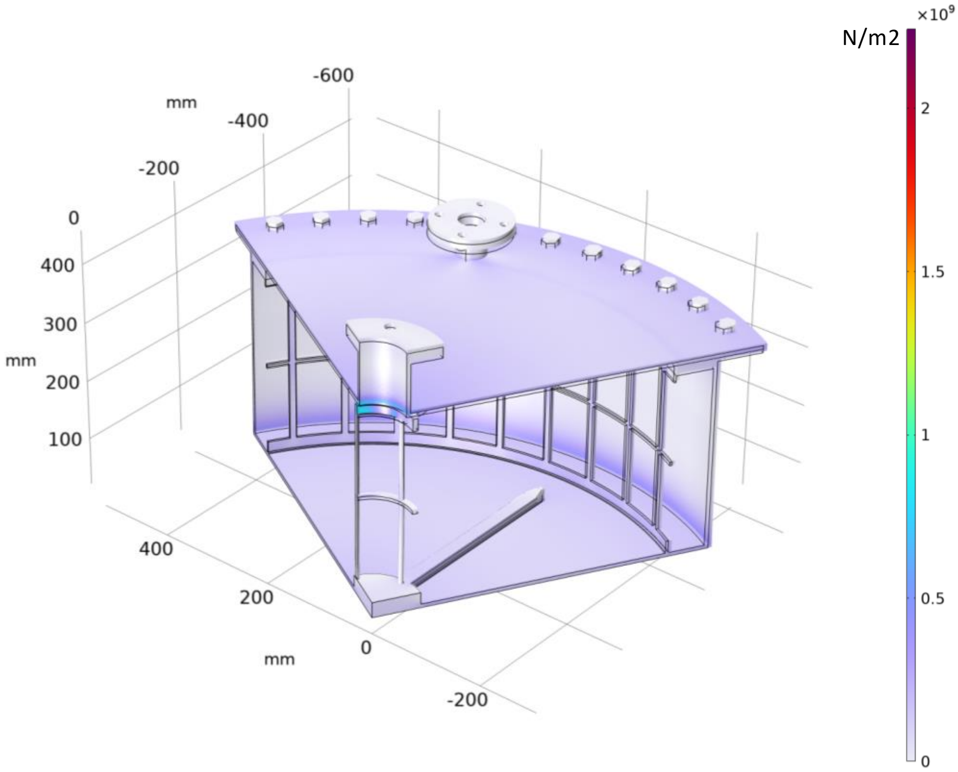

FIGURE 34: VON MISES STRESS RESULTS FOR THE OPERATION OF PBTES, UP TO 800 C. 1/4 OF THE FULL TANK IS DESPLAYED

5. TES LAB SCALE PROTOTYPE PRELIMINARY DESIGN AND MAIN SIZING

Based on the preliminary TES thermodynamic performance results, a final TES prototype design has been defined. Table 9 summarizes the main results, while Figure 35 illustrates the final CAD version of the PBTES tank.

TABLE 9: MAIN SIZING PARAMETERS FOR THE LAB SCALE PBTES PROTOTYPE

Parameter	**Value**	**Unit**
Energy capacity	50	kWh
Maximum temperature	800	°C
Minimum temperature	350	°C
Void fraction	0.38	-
Preliminary efficiency	0.85	-
TES PB volume	0.19	m^3
TES aspect ratio ΔR/H	***1.015***	***-***
In/Out layer ratio (LR)	***0.3-0.7 (adjustable)***	***-***
Inner particle diameter (dp1)	***10-13-16***	***mm***

Outer particle diameter (dp2)	***3-6***	***mm***
TES inner pipe diameter	0.12	m
TES delta radius	0.338	m
TES outer pipe diameter	1.06	m
TES height	0.33	m
TES weight	637	kg

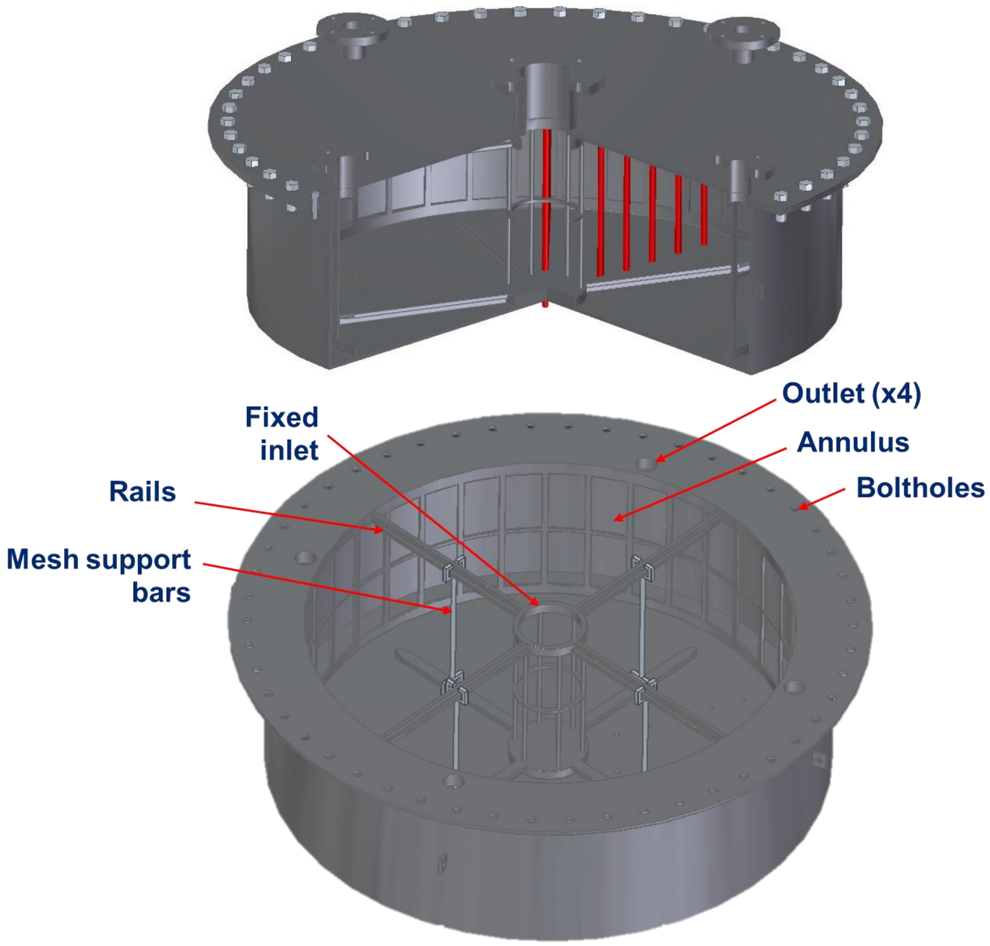

FIGURE 35: CAD OF THE PBTES FINAL GEOMETRY

The PBTES consists of two concentric cylinders: the outer wall and the outer mesh support structure. Within these, the outer annulus collects the HTF (air) before exiting the tank through four outlets. Air enters the TES via the central pipe and diffuses radially into the packed bed during charging, with the flow profile reversing during discharging. Inside the TES tank, the volume defined between the inlet area and the outer mesh support structure, is occupied by the solid fillere particles. The fixed inlet structure is upheld by thin bars around the perimeter and four rails extending from the top of the inlet structure to the outer mesh support wall. These bars are shielded by a thin mesh to prevent solid filler particles from collapsing into the inlet area. A similar mesh along the outer support wall prevents particles from entering the annulus. The four rails also support 'mesh support bars', which are in turn attached to a thin mesh acting as a layer separator. The mesh support bars and the mesh can freely move along the radius, varying the posistion of the layer separator and thus the size of the two particles layers. This design enhances the TES rig's flexibility by enabling the layer separator to adjust radially giving the opportunity to test several layer sizes. The tank's top is flat and detachable, resembling a large flange, allowing for easier loading and unloading of particles, thus improving overall functionality and accessibility. A gasket ensures a secure seal between the main tank body and the top lid. Thermocouples welded to the tank's bottom provide temperature data at 50 locations within the packed bed.

Inlet and outlet pipes welded to the top lid are connected to the rest of the piping using the installed flanges, optimizing space and simplifying the piping arrangement, since the CFD anaysis performed for the 4 geometries shown in Figure 36 did not produce significantly different results. The full piping arrangement is presented in Figure 31 and consists of 4 main valves. The different flow directions are highlighted in the Figure and correspond to the charge and discharge processes.

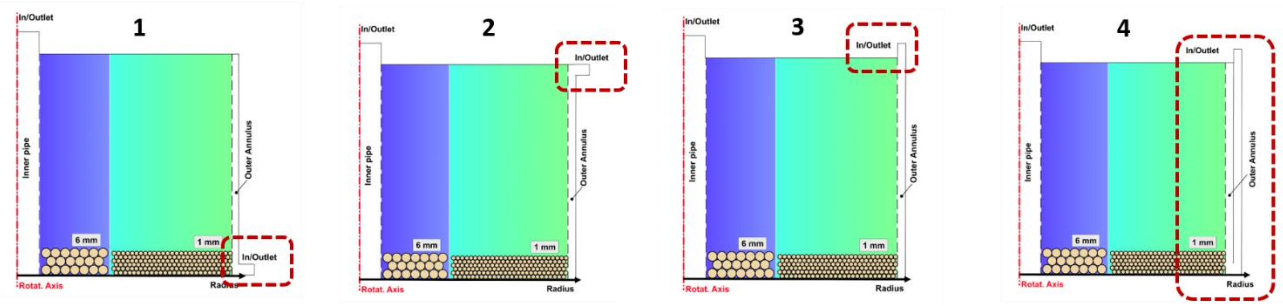

FIGURE 36: PRELIMINARY TES PROTOTYPE GEOMETRIES

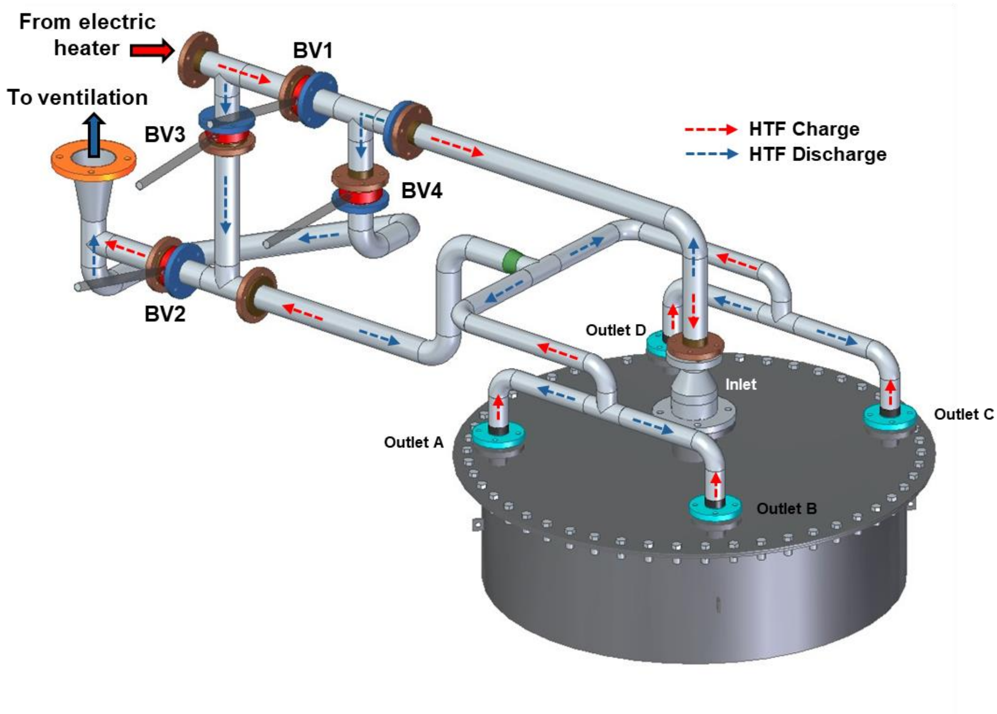

FIGURE 37: KTH'S HIGH TEMPERATURE TES RIG PIPING ARRANGEMENT

5.1. KTH TES LABORATORY RIG

The schematic layout, including the main components and the flow direction during operation, is shown in Figure 38. The rig would leverage the existing facility at KTH including the high temperature air loop and an existing low voltage electric heater (EH-LV). The EH-LV will be exploited to increase the air inlet temperature (coming at ambient conditions) up to the designed minimum temperature during discharge and up to inlet temperature during charge. A set of 4 butterfly valves (BV) (already existent within the KTH's rig, and whose arrangement is shown in Figure 38) will be used to revert the inlet/outlet fluid flow direction during charge and discharge. The system also includes a mass flow controller and a pressure relief valve to avoid accidental pressure buildup, outside the design operating conditions in the TES. The outflow of the system will be directed to the ventilation system and subsequently outside the building. Several pressure sensors will also be accommodated in the system including: before the EH, before the TES inlet at the top and after each one of the four outlets.

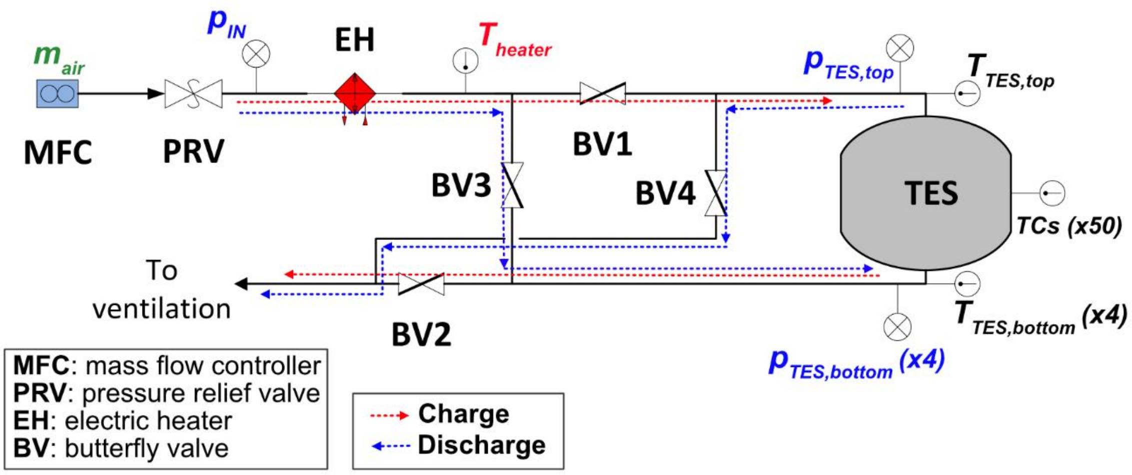

FIGURE 38: KTH'S HIGH TEMPERATURE RIG SCHEMATIC LAYOUT INCLUDING BUTTERFLY VALVES ARRANGEMENT

5.2. SOLID FILLER MATERIALS

Several solid filler materials are being investigated in order to assess their suitability for usage in the PBTES. Some of the materials considered include commercial ceramics, copper slags, brass slags, steel slags, waste roof tiles, waste bricks and clinker from ceramic waste. The aforementioned materials will be first characterized in the laboratory in order to assess their main thermodynamic and physical properties. The main properties to be identified and tests that will be performed include:

- Thermal cycling (TGA)
- Specific heat capacity (DSC)
- Thermal conductivity (TPS)
- Linear thermal expansion (Dilatometer test)
- Density (Fluid displacement method)
- Hardness (Vickers test)

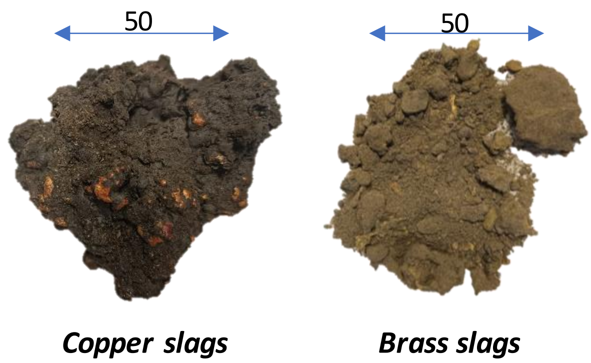

FIGURE 39: PHOTOGRAPHS OF COPPER AND BRASS SLAGS SAMPLES

Most of the materials taken into account are industrial byproducts or wastes that originate from different industries or processes (ceramic and metallic material industries). Therefore, the elemental analysis of them is expected to vary significantly. However, all materials are expected to have high specific heat capacity and relatively high density according to literature which makes them excellent candidates for TES as shown in Table 10.

TABLE 10: LITERATURE VALUES FOR DENSITY AND SPECIFIC HEAT CAPACITY OF SELECTED MATERIALS

Property/Solid filler	Comm. ceramic	Steel slags	Copper slags
Density [kg/m3]	2097	3500	3600
Specific heat capacity [J/kgK]	820	950	1300
References	[17,33]	[34]	[35]

The different origin of the materials also leads to very different macroscopic properties such as mean particle diameter and fragility. It can be observed in Figure 39 that copper and brass slags are significantly different since copper slags consist of rigid particles of around 50 mm in diameter while brass slags are fragile in a powder form which can be a great bottleneck for usage in the PBTES. After characterizing the various materials in the lab, the goal is to use the most suitable ones as solid fillers in the PBTES prototype and perform numerous experiments, that can be facilitated due to the innovative and flexible design of the prototype which is expected to simplify the processes of loading and unloading.

6. TES UPSCALED CONCEPTS – PRELIMINARY INDENTIFICATION

As previously mentioned, the TES prototype design as well as the identification of the key features to test and validate at laboratory scale during the experimental campaign in WP4 is ongoing largely taking into account the potential upscaling of the proposed TES. Such upscaling will carry along additional challenges that has to be considered and possibly verified during the prototyping phase.

When upscaling packed bed TES a major issue is represented by the thermomechanical interaction between the storage tank and the filler material. The proposed radial configuration in which the outer region is kept at lower temperature should limit this problem reducing the temperature variations faced by the TES walls. However, such behaviour will be further examined via dedicated CFD aimed at better investigating the TES thermal ratcheting in radial packed bed TES units. With this in mind the maximum TES size will be determined mostly based on the stressed faced by the tank.

A first simple upscaling strategy for the proposed TES is based on the initial concept including three annular layers (sketched in Figure 40 on the left). The three layers would have limited influence and involve high manufacturability complications in the lab scale TES, thus they would likely not be installed in the prototype. However, CFD models validated based on a 2 layers TES can easily be extended and applied to a 3 layers system. Indeed, all the key features relative to particles and fluid interaction are already covered and fully investigated. Such up-scaled TES would provide a simpler installation, operation and maintenance; however the upscaling would be limited by thermal ratcheting and thermos-mechanical stresses. While evaluating this upscaling strategy a horizontal configuration will be also assessed. In this approach the rotational axis will be horizontal. The thermal performance are expected to be worse, and thermal stratification is expected to appear. However, such arrangement might simplify the piping connections ensuring easier installation particularly for systems including multiple TES units.

Alternatively, an up-scaled TES unit involving a truncated conical main TES vessel and inner pipe is considered (sketched in Figure 40 on the left). This solution also relies on burying the unit into the ground. The truncated conical scape of the TES, as shown by Zanganeh, can limit the thermal ratcheting phenomena promoting and upward movement of the particles. Such arrangement could therefore maximize the upscaling limit and permit larger single unit TES installations. Additional, a buried tank could permit to utilize (at least partially) the above ground limiting the footprint and increasing the compactness of the system (feature that might not be extremely relevant for CSP plants but might be interesting for other component related exploitation opportunities). Generally, such arrangement has a more complicated operation and maintenance due to the difficulty in accessing the TES and it also introduce costs for the excavation. However, the current proposed innovative PBTES could deal with this issue, if upscaled, since all piping is located on the top of the tank and the inner parts of the tank are easily accessible for inspection and maintenance purposes.

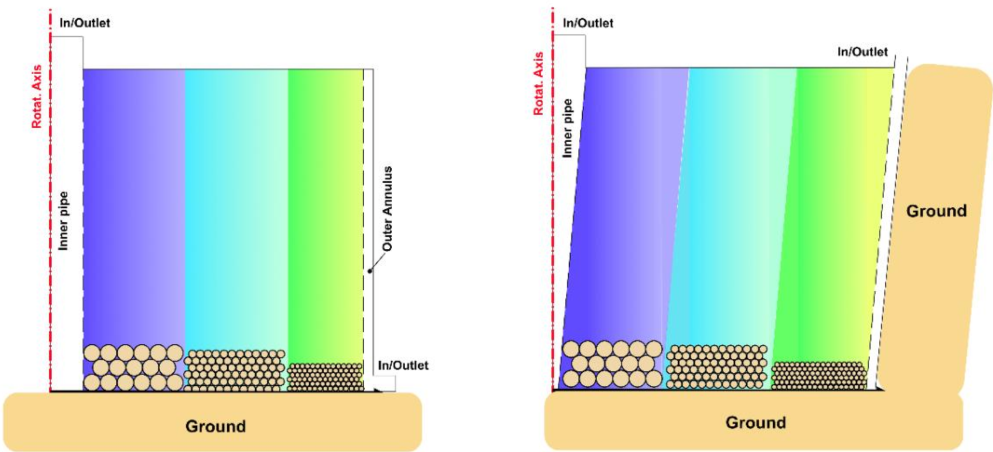

FIGURE 40: TES UPSCALED PRELIMINARY CONCEPTS

Figure 41 is illustrating the energy capacity of different PBTES systems with respect to the area they require and the aspect ratio of the PB. It is evident that PBs with axial orientation require significantly smaller area than radial PBs in order to store the same energy content. However, radial PBTES is still competitive if the correct aspect ratios are selected in large scale units and even outperforms existing molten salt storage systems, in terms of space requirements. Overall, it is evident that axial and radial designs both perform

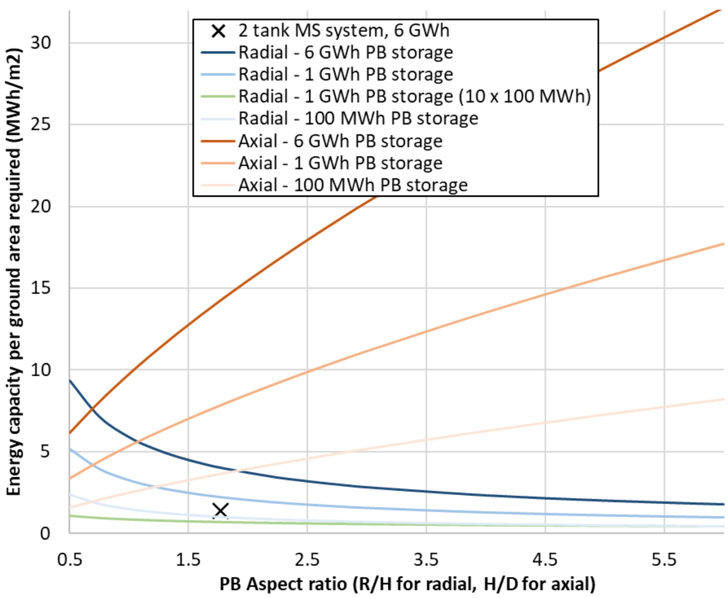

FIGURE 41: SIZE COMPARISON BETWEEN AXIAL AND RADIAL PBS.

better in this indicator when the system size is increased and only one tank is used for storage. For example, when comparing a 1 GWh radial TES unit that consists of 10 tanks of 100 MWh with a 1 GWh one-tank TES unit, the former one is able to store 3 times less energy given the same available area, especially for low aspect ratios.

Additionally, a last preliminary TES upscaling concept is sketched in Figure 42. As described in Section 4, higher aspect ratios (meaning larger and shorter TES) might lead to better thermal performance (longer useful operation periods) with limited pressure drop increases. Therefore up-scaled TES with wider radius seems more profitable. To attain a full TES upscaling with high aspect ratio, a system made of vertically stacked TES is shown. This stacking approach could ensure good thermal performance, still limiting the footprint of the TES. Additionally, an increased modularity and flexibility of the full system could be achieved. This characteristic could not only facilitate its manufacturability but also improve the TES performance during off-design operation. Specifically when low HTF flow rates would be operated only some of the TES units could be activated still attaining relevant flow speed and heat transfer coefficients between fluid and particles. There operational window of the full TES system could be extended. However, this upscaling strategy would require additional costs and complexity due to the need for an external support structure and external piping arrangement ensuring a proper flow distribution among the different TES units. To assess the suitability of such upscaling approach dedicated CFD and cost assessment will be carried out. Specifically, the influence of the aspect ratio will be detailed also for up-scaled TES units.

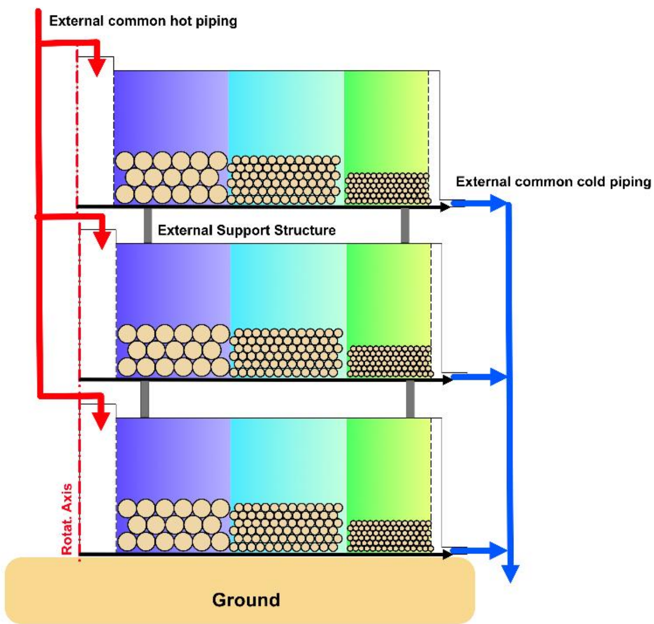

FIGURE 42: MODULAR TES UPSCALED PRELIMINARY CONCEPT

7. CONCLUSIONS

This deliverable describes the optimized design of the high temperature radial flow packed bed thermal energy storage as part of WP4.

Specifically, the below points have been addressed:

- A summary of the considered boundary conditions for the storage prototype and up-scaled unit accounting for the cyber-physical lab integration (and following the work of T5.1) and relative limitations and capabilities of the KTH's experimental facility.

- A review of the existing high temperature packed bed thermal energy storage design concepts
- A description of the main characteristics of the proposed storage concept and how these would address the main shortcomings and drawbacks of state-of-the-art solutions.
- A description of the methodology and modelling approach (1/2/3D also via dedicated CFD/FEM) followed to evaluate the thermo-, hydrodynamic and thermomechanical performance of the proposed storage and identify the main characteristics and feature of the lab prototype.
- The main outcomes for the different modelling activities and design optimizations leading to the finalized TES units design which is shown to be representative of upscaled systems.
- Key results focused on thee expected thermodynamic behaviour of the TES unit and the relevance of key design parameters, the fluido-dynamic performance of the system and the TES geometrical optimization to ensure optimal flow distribution, as well as the thermos-mechanical analysis of the unit.
- The finalized TES prototype design is described and examples of the main drawings for TES manufacturing are provided.
- A preliminary description of the TES/EH laboratory rig and the ongoing planning and adaptation activities
- A description of potential TES up-scaled solutions that will serve as a basis for the upcoming detailed CFD/FEM assessment and provide specifications on the main features to be validated during the experimental campaign.

This work covers all major steps leading to the finalized TES design toward performance optimization and leads to way to prototyping and validation work which will be carried on in the next tasks of WP4.

REFERENCES

[1] Trevisan S, Guédez R, Laumert B. Thermo-economic optimization of an air driven supercritical CO2 Brayton power cycle for concentrating solar power plant with packed bed thermal energy storage. Sol Energy 2020;211:1373–91. https://doi.org/10.1016/j.solener.2020.10.069.

[2] Zanganeh G, Pedretti A, Zavattoni S, Barbato M, Steinfeld A. Packed-bed thermal storage for concentrated solar power - Pilot-scale demonstration and industrial-scale design. Sol Energy 2012;86:3084–98. https://doi.org/10.1016/j.solener.2012.07.019.

[3] Zanganeh G, Pedretti A, Haselbacher A, Steinfeld A. Design of packed bed thermal energy storage systems for high-temperature industrial process heat. Appl Energy 2015;137:812–822. https://doi.org/10.1016/j.apenergy.2014.07.110.

[4] Avila-Marin AL, Alvarez-Lara M, Fernandez-Reche J. A regenerative heat storage system for central receiver technology working with atmospheric air. Energy Procedia, 2013. https://doi.org/10.1016/j.egypro.2014.03.076.

[5] Haller MY, Cruickshank CA, Streicher W, Harrison SJ, Andersen E, Furbo S. Methods to determine stratification efficiency of thermal energy storage processes - Review and theoretical comparison. Sol Energy 2009. https://doi.org/10.1016/j.solener.2009.06.019.

[6] Geissbühler L, Mathur A, Mularczyk A, Haselbacher A. An assessment of thermocline-control methods for packed-bed thermal-energy storage in CSP plants, Part 1: Method descriptions. Sol Energy 2019;178:341–50. https://doi.org/10.1016/j.solener.2018.12.015.

[7] Al-azawii MMS, Theade C, Danczyk M, Johnson E, Anderson R. Experimental study on the cyclic behavior of thermal energy storage in an air-alumina packed bed. J Energy Storage 2018;18:239–49. https://doi.org/10.1016/j.est.2018.05.008.

[8] Nsofor EC. Investigations on the Packed Bed for High-Temperature Thermal Energy Storage. Int J

Green Energy 2005. https://doi.org/10.1080/01971520500287925.

[9] Klein P, Roos TH, Sheer TJ. Experimental investigation into a packed bed thermal storage solution for solar gas turbine systems. Proc. SolarPACES 2013 Int. Conf., 2014, p. 840–9. https://doi.org/10.1016/j.egypro.2014.03.091.

[10] Zanganeh G, Khanna R, Walser C, Pedretti A, Haselbacher A, Steinfeld A. Experimental and numerical investigation of combined sensible-latent heat for thermal energy storage at 575°C and above. Sol Energy 2015. https://doi.org/10.1016/j.solener.2015.01.022.

[11] Geissbühler L, Kolman M, Zanganeh G, Haselbacher A, Steinfeld A. Analysis of industrial-scale high-temperature combined sensible/latent thermal energy storage. Appl Therm Eng 2016;101:657–68. https://doi.org/10.1016/j.applthermaleng.2015.12.031.

[12] Gauché P. South African provisional patent application. 2014/03555, 2014.

[13] Allen K, Von Backström T, Joubert E, Gauché P. Rock bed thermal storage: Concepts and costs. AIP Conf. Proc., 2016. https://doi.org/10.1063/1.4949101.

[14] Laubscher HF, Von Backström TW, Dinter F. Developing a cost effective rock bed thermal energy storage system: Design and modelling. AIP Conf. Proc., 2017. https://doi.org/10.1063/1.4984436.

[15] Schlipf D, Faust E, Schneider G, Maier H. First operational results of a high temperature energy storage with packed bed and integration potential in CSP plants. AIP Conf. Proc., 2017. https://doi.org/10.1063/1.4984445.

[16] Faust E, Schlipf D, Schneider G, Maier H. Flow modeling of a packed bed high temperature thermal energy storage system. AIP Conf Proc 2018;2033:1–8. https://doi.org/10.1063/1.5067102.

[17] Trevisan S, Wang W, Guedez R, Laumert B. Experimental Evaluation of an Innovative Radial-Flow High-Temperature Packed Bed Thermal Energy Storage. Appl Energy 2022;311. https://doi.org/10.1016/j.apenergy.2022.118672.

[18] Daschner R, Binder S, Mocker M. Pebble bed regenerator and storage system for high temperature use. Appl Energy 2013;109:394–401. https://doi.org/10.1016/j.apenergy.2012.10.062.

[19] Biencinto M, Bayón R, Rojas E, González L. Simulation and assessment of operation strategies for solar thermal power plants with a thermocline storage tank. Sol Energy 2014;103:456–72. https://doi.org/10.1016/j.solener.2014.02.037.

[20] Walmsley MRW, Atkins MJ, Riley J. Thermocline Management of Stratified Tanks for Heat Storage. 12th Int. Conf. Process Integr. Model. Optim. Energy Sav. Pollut. Reduct., 2009, p. 231–6.

[21] Bindra H, Bueno P, Morris JF. Sliding flow method for exergetically efficient packed bed thermal storage. Appl Therm Eng 2014;64:201–8. https://doi.org/10.1016/j.applthermaleng.2013.12.028.

[22] Mathur AK, Kasetty RB. Thermal Energy Storage System Compromising Optimal Thermocline Management. US 8,554,377 B2, 2013.

[23] Schumann TEW. Heat transfer: A liquid flowing through a porous prism. J Franklin Inst 1929. https://doi.org/10.1016/S0016-0032(29)91186-8.

[24] Coutier JP, Farber EA. Two applications of a numerical approach of heat transfer process within rock beds. Sol Energy 1982;29:451–62. https://doi.org/10.1016/0038-092X(82)90053-6.

[25] Esence T, Bruch A, Molina S, Stutz B, Fourmigué JF. A review on experience feedback and numerical modeling of packed-bed thermal energy storage systems. Sol Energy 2017. https://doi.org/10.1016/j.solener.2017.03.032.

[26] Kunii D, Smith JM. Heat Transfer Characteristics of Porous Rocks. AIChE J 1960;6:71–8.

https://doi.org/doi.org/10.1002/aic.690060115.

[27] Cheng P, Hsu C-T. Heat Conduction. Transp. Phenom. Porous Media, Pergamon; 1998, p. 57–76. https://doi.org/10.1016/B978-0-08-042843-7.50003-9.

[28] Ergun S, Orning AA. Fluid Flow through Randomly Packed Columns and Fluidized Beds. Ind Eng Chem 1949;41:1179–84. https://doi.org/10.1021/ie50474a011.

[29] Fischer RA. Statistical Methods for Research Workers. 1958.

[30] Lule SS, Asaditaheri A. Computational Fluid Dynamics Analysis of a Thermocline Thermal. Arab J Sci Eng 2022;47:9005–18. https://doi.org/10.1007/s13369-021-06485-8.

[31] Elsayed K, Abubakar E, Mohammed G. Performance analysis of an air rock thermocline TES tank for concentrated solar power plants using the coupled DEM – CFD approach. Clean Technol Environ Policy 2022;24:3–19. https://doi.org/10.1007/s10098-021-02030-1.

[32] Cascetta M, Cau G, Puddu P, Serra F. A comparison between CFD simulation and experimental investigation of a packed-bed thermal energy storage system. Appl Therm Eng 2016;98:1263–72. https://doi.org/10.1016/j.applthermaleng.2016.01.019.

[33] Saint-Gobain NORPRO. Denstone Support Media. 2020.

[34] Ortega-Fernández I, Rodríguez-Aseguinolaza J. Thermal energy storage for waste heat recovery in the steelworks: The case study of the REslag project. Appl Energy 2019;237:708–19. https://doi.org/10.1016/j.apenergy.2019.01.007.

[35] Calderón-Vásquez I, Segovia V, Cardemil JM, Barraza R. Assessing the use of copper slags as thermal energy storage material for packed-bed systems. Energy 2021;227. https://doi.org/10.1016/j.energy.2021.120370.

APPENDIX A

Material Properties

Properties of interest of the materials used in the TES system investigation are presented in the following figures and tables.

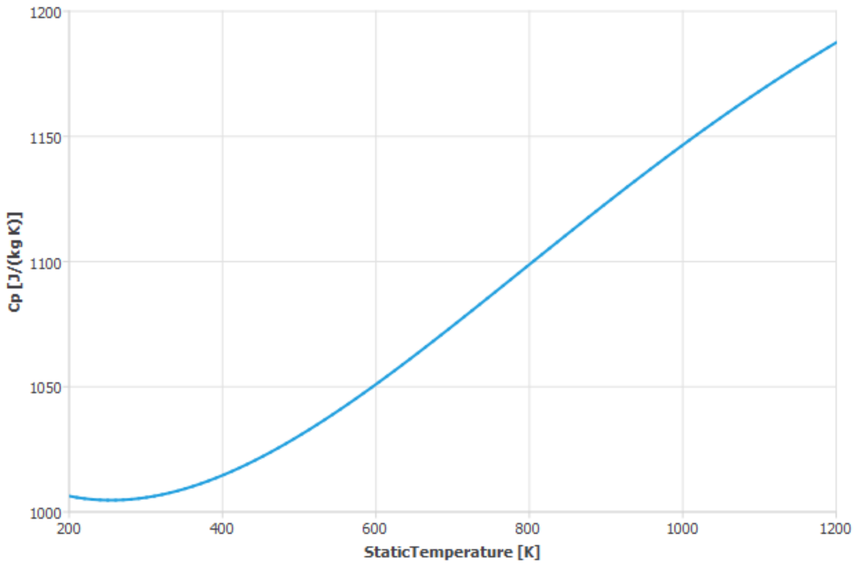

FIGURE 43. ISOBARIC SPECIFIC HEAT CAPACITY OF AIR AS A FUNCTION OF TEMPERATURE.

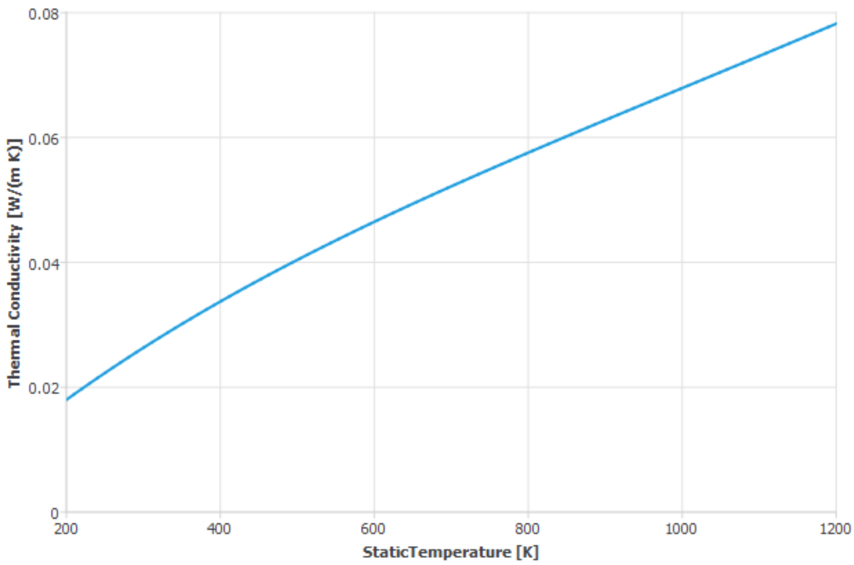

FIGURE 44. THERMAL CONDUCTIVITY OF AIR AS A FUNCTION OF TEMPERATURE.

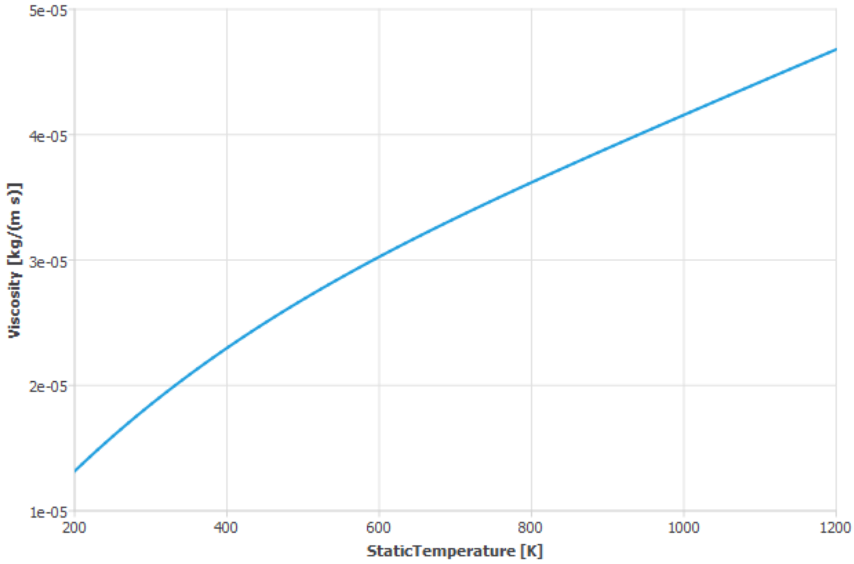

FIGURE 45. VISCOSITY OF AIR AS A FUNCTION OF TEMPERATURE.

TABLE 11. DENSITY OF INCONEL-625 AS A FUNCTION OF TEMPERATURE.

Validity range, T [K]	Density [kg m^{-3}]
19 ≤ T < 63	$8307.731 + 0.02514403 * T - 5.796501 \times 10^{-4} * T^2 - 2.905535 \times 10^{-6} * T^3$
63 ≤ T < 250	$8308.627 + 0.0376521 * T - 12.56698 \times 10^{-4} * T^2 + 1.529227 \times 10^{-6} * T^3$
250 ≤ T < 1200	$8339.072 - 0.3000351 * T + 2.796812 \times 10^{-6} * T^2 - 5.001998 \times 10^{-8} * T^3$

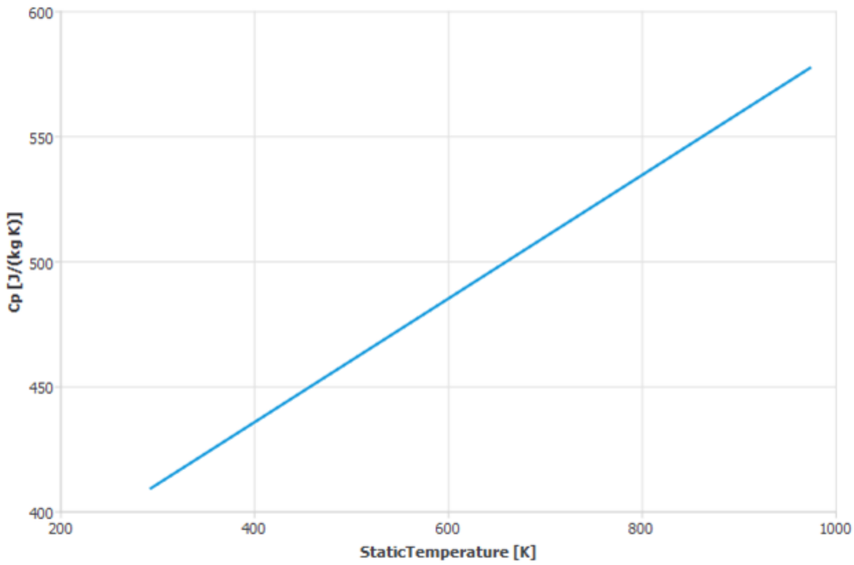

FIGURE 46. ISOBARIC SPECIFIC HEAT CAPACITY OF INCONEL-625 AS A FUNCTION OF TEMPERATURE.

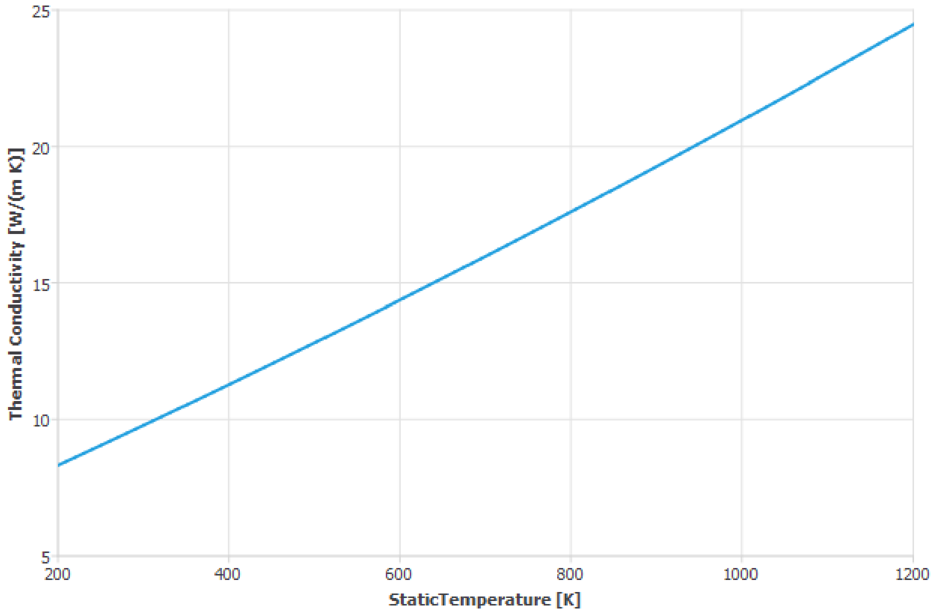

FIGURE 47. THERMAL CONDUCTIVITY OF INCONEL-625 AS A FUNCTION OF TEMPERATURE.

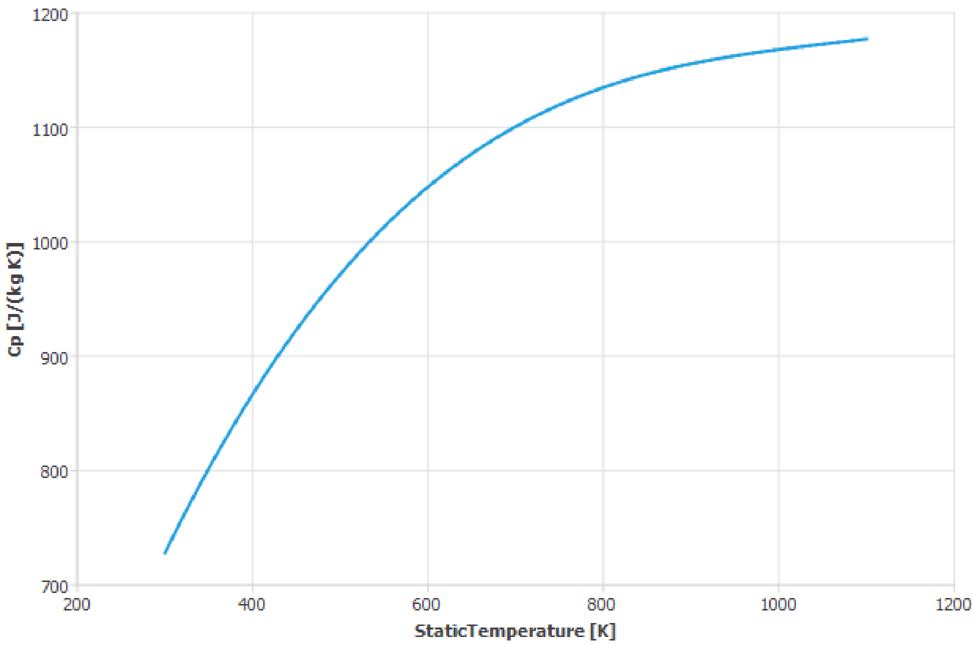

FIGURE 48. ISOBARIC SPECIFIC HEAT CAPACITY OF DENSTONE® 2000 AS A FUNCTION OF TEMPERATURE.

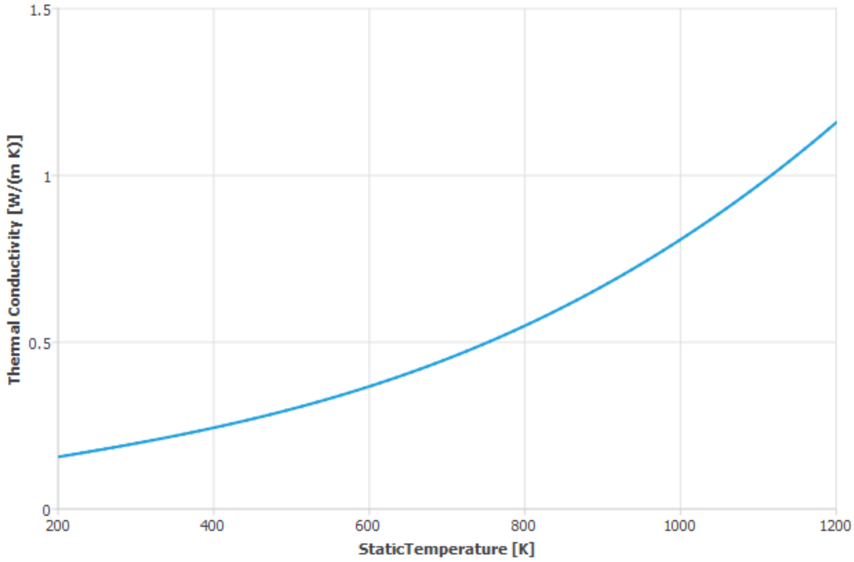

FIGURE 49. THERMAL CONDUCTIVITY OF DENSTONE® 2000 AS A FUNCTION OF TEMPERATURE.

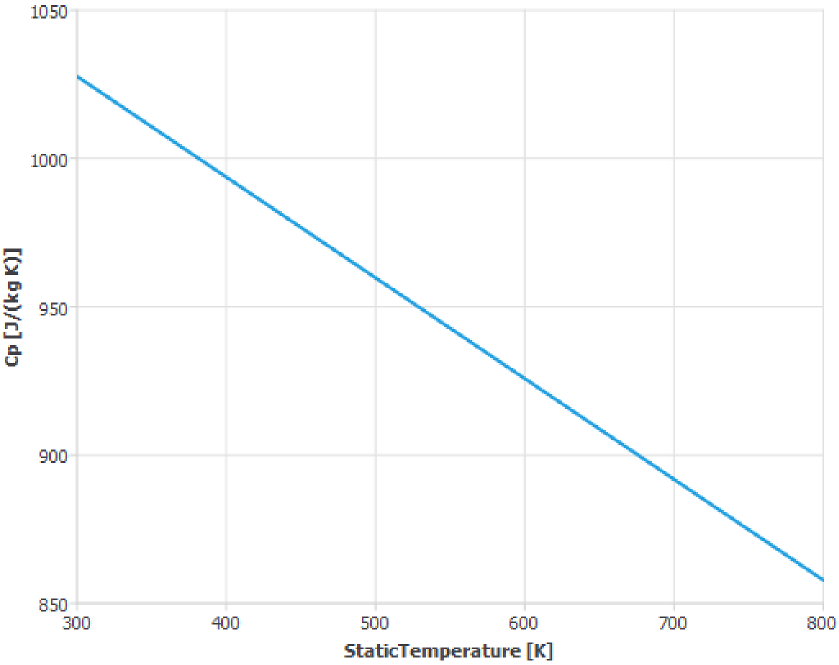

FIGURE 50. ISOBARIC SPECIFIC HEAT CAPACITY OF THE SECOND LAYER OF INSULATION AS A FUNCTION OF TEMPERATURE.

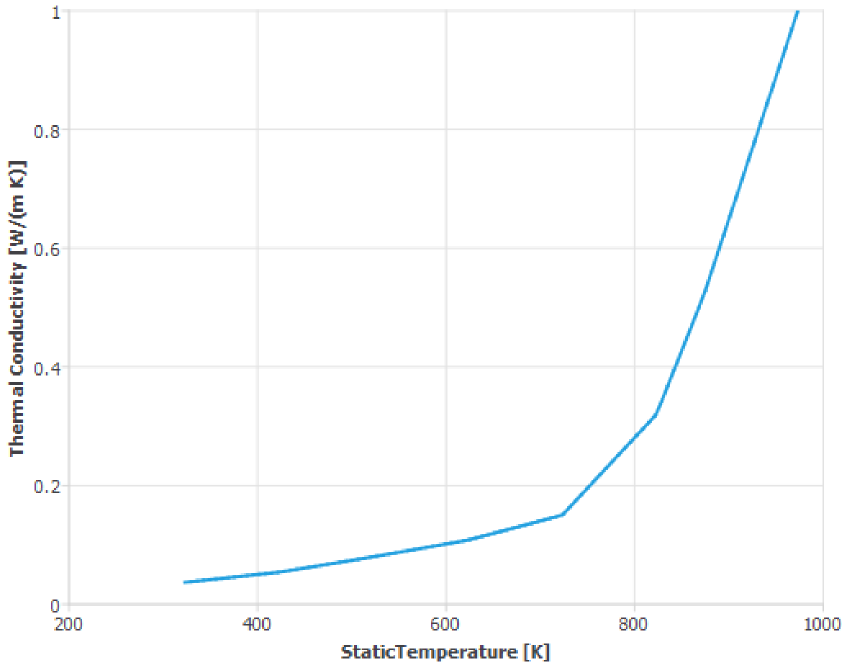

FIGURE 51. THERMAL CONDUCTIVITY OF THE SECOND LAYER OF INSULATION AS A FUNCTION OF TEMPERATURE.